Scale-by-scale non-equilibrium with Kolmogorov-like scalings in non-homogeneous stationary turbulence

Paul Beaumard, Pierre Bragança, Christophe Cuvier, Konstantinos Steiros, John Christos Vassilicos

Scale-by-scale non-equilibrium with Kolmogorov-like scalings in non-homogeneous stationary turbulence

P. Beaumard [1], P. Bragança [1], C. Cuvier [1], K. Steiros [2] and J.C Vassilicos [1]†

[1]Univ. Lille, CNRS, ONERA, Arts et Metiers Institute of Technology, Centrale Lille, UMR 9014 - LMFL - Laboratoire de Mécanique des Fluides de Lille - Kampé de Fériet, F-59000 Lille, France

[2]Department of Aeronautics, Imperial College London, London SW7 2AZ, United Kingdom

(Received 13 June 2023; revised xx; accepted xx)

An improved version of the non-equilibrium theory of non-homogeneous turbulence of Chen & Vassilicos (2022) predicts that an intermediate range of length-scales exists where the interscale turbulence transfer rate, the two-point interspace turbulence transport rate and the two-point pressure gradient velocity correlation term in the two-point small-scale turbulent energy equation are all proportional to the turbulence dissipation rate and independent of length-scale. Particle Image Velocimetry (PIV) measurements in a field of view under the turbulence-generating impellers in a baffled water tank support these predictions and show that the measured small-scale turbulence is significantly non-homogeneous. The PIV measurements also suggest that the rate with which large scales lose energy to the small scales in the two-point large-scale turbulent energy equation behaves in a similar way and that this rate may not balance the interscale turbulence transfer rate in the two-point small-scale turbulent energy equation because of turbulent energy transport caused by the non-homogeneity.

Key words: Turbulence theory, Particle Image Velocimetry, Mixing tank

1. Introduction

The Kolmogorov 1941 theory of statistically homogeneous turbulence (see Frisch (1995), Pope (2000)) predicts that the interscale transfer rate of turbulent kinetic energy is approximately balanced by the turbulence dissipation rate across a wide range of length scales in the inertial range as the Reynolds number tends to infinity. This prediction of scale-by-scale equilibrium holds for statistically stationary forced homogeneous turbulence (see Frisch (1995)) but is also made for decaying homogeneous turbulence on the basis of a small-scale stationarity hypothesis (see Frisch (1995), Pope (2000) and section 2 of Chen & Vassilicos (2022)). A widely held view is that the turbulence is always statistically homogeneous at small enough length-scales if the Reynolds number is large enough. But what if the Reynolds

† Email address for correspondence: john-christos.vassilicos@cnrs.fr

number, even if high, is not high enough for homogeneity to exist at the smallest scales? And if, in such circumstances, one finds simple scalings and scale-by-scale balances which appear independent of the details of the non-homogeneity, would these non-homogeneity laws survive as the Reynolds is taken to infinity? Or would they locally tend to Kolmogorov scale-by-scale equilibrium, in which case Kolmogorov scale-by-scale equilibrium would, in some sense, be an asymptotic case of these non-homogeneity laws?

In this paper we address statistically stationary non-homogeneous turbulence at moderate to high Reynolds numbers and we attempt to provide some partial answer to the first one of these questions: can simple scale-by-scale turbulence energy balances exist in non-homogeneous turbulence? The questions concerning the limit towards infinite Reynolds numbers cannot be answered at present and may, perhaps, never be answered unless one can some day answer them by rigorous mathematical analysis of the Navier-Stokes equations. The problem with claims made for Reynolds numbers tending to infinity is that one can always argue that the Reynolds number is not large enough if an experiment or simulation does not confirm the claims.

We chose to study the turbulent flow under the turbulence-generating rotating impellers in a baffled tank where the baffles break the rotation of the flow. This is a flow where the turbulence is statistically stationary, where Taylor length-based Reynolds numbers up to order 10^3 can be achieved, where different types of impeller can produce significantly different turbulent flows and where we can use a two-dimensional two-component (2D2C) Particle Image Velocimetry (PIV) that is highly resolved in space and capable to access estimates of turbulence dissipation rates as well as parts of various interscale and interspace turbulent transfer/transport rates. Only full three-dimensional three-component highly resolved PIV measurements can, in principle, access the turbulence dissipation and these transfer/transport rates in full, but such an approach is currently beyond our reach over the significant range of length scales needed to establish scale-by-scale energy balances. The truncated transfer/transport rates obtained by our 2D2C PIV do, nevertheless, exhibit interesting properties, in particular because they are concordant with a recent non-equilibrium theory of non-homogeneous turbulence (Chen & Vassilicos (2022)) which we also further develop here.

In the following section we present the two-point scale-by-scale equations which form the basis of this study's theoretical framework. In section 3, we discuss interscale turbulent energy transfers and the special case of freely decaying statistically homogeneous turbulence as a point of reference. Section 4 presents the experiment apparatus and the 2D2C PIV. We use our PIV measurements to assess two-point turbulence production in section 5 and linear transport terms (e.g. mean advection) in section 6. In section 7 we present intermediate similarity predictions and PIV measurements of second order structure functions of turbulent fluctuating velocities. Section 8 presents theoretical predictions of non-equilibrium small-scale turbulent energy budgets for non-homogeneous turbulence and related 2D2C PIV measurements. Finally, section 9 presents measurements and a theoretical discussion of elements of the large-scale turbulent energy budget, section 10 proposes a small-scale homogeneity hypothesis and we conclude in section 11.

2. Theoretical framework based on two-point Navier-Stokes equations

Interscale turbulence transfers for incompressible turbulence can be studied in the presence of all other co-existing turbulence transfer/transport mechanisms in terms of two-point equations exactly derived from the incompressible Navier-Stokes equations (see Hill (2001), Hill (2002) and Germano (2007)) without any hypotheses or assumptions, in particular no assumptions of homogeneity or periodicity. The incompressible Navier-Stokes equation is written at two points $\boldsymbol{\zeta}^- = \boldsymbol{X} - \boldsymbol{r}$ and $\boldsymbol{\zeta}^+ = \boldsymbol{X} + \boldsymbol{r}$ in physical space (see figure 1) where $\boldsymbol{X}$ is the centroid

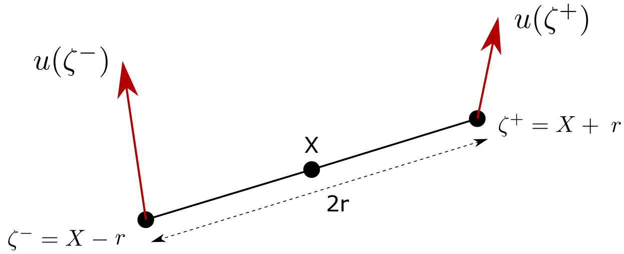

Figure 1: Schematic of fluid velocities at points $\boldsymbol{\zeta}^- = \boldsymbol{X} - \boldsymbol{r}$ and $\boldsymbol{\zeta}^+ = \boldsymbol{X} + \boldsymbol{r}$.

and $2\boldsymbol{r}$ is the two-point separation vector. One defines the two-point velocity half difference $\boldsymbol{\delta u}(\boldsymbol{X},\boldsymbol{r},t) \equiv \frac{\boldsymbol{u}^+ - \boldsymbol{u}^-}{2}$ where $\boldsymbol{u}^+ \equiv \boldsymbol{u}(\boldsymbol{\zeta}^+)$ and $\boldsymbol{u}^- \equiv \boldsymbol{u}(\boldsymbol{\zeta}^-)$ are the fluid velocities at each one of the two points and the two-point pressure half difference $\delta p(\boldsymbol{X},\boldsymbol{r},t) \equiv \frac{p^+ - p^-}{2}$ where $p^+ \equiv p(\boldsymbol{\zeta}^+)$ and $p^- \equiv p(\boldsymbol{\zeta}^-)$ are the pressure over density ratios at each one of the two points. Incompressibility immediately imposes $\boldsymbol{\nabla_X}.\boldsymbol{\delta u} = \boldsymbol{\nabla_r}.\boldsymbol{\delta u} = 0$ and the Navier Stokes equation implies (Hill (2001), Hill (2002))

$$\frac{\partial \boldsymbol{\delta u}}{\partial t} + (\boldsymbol{u_X}.\boldsymbol{\nabla_X})\,\boldsymbol{\delta u} + (\boldsymbol{\delta u}.\boldsymbol{\nabla_r})\,\boldsymbol{\delta u} = -\boldsymbol{\nabla_X}\delta p + \frac{\nu}{2}\boldsymbol{\nabla_X}^2\boldsymbol{\delta u} + \frac{\nu}{2}\boldsymbol{\nabla_r}^2\boldsymbol{\delta u} \tag{2.1}$$

where $\boldsymbol{u_X}(\boldsymbol{X},\boldsymbol{r},t) \equiv \frac{\boldsymbol{u}^+ + \boldsymbol{u}^-}{2}$; $\nabla_{\mathbf{X}}$ and $\boldsymbol{\nabla_X}^2$ are the gradient and Laplacian in $\mathbf{X}$ space; $\nabla_{\mathbf{r}}$ and $\boldsymbol{\nabla_r}^2$ are the gradient and Laplacian in $\mathbf{r}$ space; and ν is the kinematic viscosity.

An energy equation is readily obtained by multiplying equation 2.1 with $2\boldsymbol{\delta u}$:

$$\frac{\partial|\boldsymbol{\delta u}|^2}{\partial t} + \boldsymbol{\nabla_X}.(\boldsymbol{u_X}|\boldsymbol{\delta u}|^2) + \boldsymbol{\nabla_r}.(\boldsymbol{\delta u}|\boldsymbol{\delta u}|^2) = -2\boldsymbol{\nabla_X}.(\boldsymbol{\delta u}\delta p) + \frac{\nu}{2}\boldsymbol{\nabla_X}^2|\boldsymbol{\delta u}|^2 + \frac{\nu}{2}\boldsymbol{\nabla_r}^2|\boldsymbol{\delta u}|^2 - \frac{1}{2}\epsilon^+ - \frac{1}{2}\epsilon^- \tag{2.2}$$

where $\epsilon^+ = \nu\frac{\partial u_i^+}{\partial \zeta_k^+}\frac{\partial u_i^+}{\partial \zeta_k^+}$ and $\epsilon^- = \nu\frac{\partial u_i^-}{\partial \zeta_k^-}\frac{\partial u_i^-}{\partial \zeta_k^-}$. With a Reynolds decomposition $\boldsymbol{\delta u} = \overline{\boldsymbol{\delta u}} + \boldsymbol{\delta u}'$, $\boldsymbol{u_X} = \overline{\boldsymbol{u_X}} + \boldsymbol{u_X}'$, $\delta p = \delta\overline{p} + \delta p'$ where the overline signifies an average over time under the assumption of statistical stationarity, this general two-point energy equation leads to the following pair of two-point energy equations:

$$\begin{aligned}
&(\overline{\boldsymbol{u_X}}.\boldsymbol{\nabla_X} + \boldsymbol{\delta\overline{u}}.\boldsymbol{\nabla_r})\,\frac{1}{2}|\boldsymbol{\delta\overline{u}}|^2 + P_r + P_{Xr}^s + \frac{\partial}{\partial x_j}(\delta\overline{u_i}\overline{u'_{Xj}\delta u'_i}) + \frac{\partial}{\partial r_j}(\delta\overline{u_i}\overline{\delta u'_j\delta u'_i}) \\
&= -\boldsymbol{\nabla_X}.(\boldsymbol{\delta\overline{u}}\delta\overline{p}) + \frac{\nu}{2}\boldsymbol{\nabla_X}^2\frac{1}{2}|\boldsymbol{\delta\overline{u}}|^2 + \frac{\nu}{2}\boldsymbol{\nabla_r}^2\frac{1}{2}|\boldsymbol{\delta\overline{u}}|^2 - \frac{\nu}{4}\frac{\partial\overline{u}_i^+}{\partial\zeta_k^+}\frac{\partial\overline{u}_i^+}{\partial\zeta_k^+} - \frac{\nu}{4}\frac{\partial\overline{u}_i^-}{\partial\zeta_k^-}\frac{\partial\overline{u}_i^-}{\partial\zeta_k^-}
\end{aligned} \tag{2.3}$$

$$\begin{aligned}
&(\overline{\boldsymbol{u_X}}.\boldsymbol{\nabla_X} + \boldsymbol{\delta\overline{u}}.\boldsymbol{\nabla_r})\,\frac{1}{2}\overline{|\boldsymbol{\delta u}'|^2} - P_r - P_{Xr}^s + \boldsymbol{\nabla_X}.\overline{(\boldsymbol{u_X}'\frac{1}{2}|\boldsymbol{\delta u}'|^2)} + \boldsymbol{\nabla_r}.\overline{(\boldsymbol{\delta u}'\frac{1}{2}|\boldsymbol{\delta u}'|^2)} \\
&= -\boldsymbol{\nabla_X}.\overline{(\boldsymbol{\delta u}'\delta p')} + \frac{\nu}{2}\boldsymbol{\nabla_X}^2\frac{1}{2}\overline{|\boldsymbol{\delta u}'|^2} + \frac{\nu}{2}\boldsymbol{\nabla_r}^2\frac{1}{2}\overline{|\boldsymbol{\delta u}'|^2} - \frac{\nu}{4}\overline{\frac{\partial u_i'^+}{\partial\zeta_k^+}\frac{\partial u_i'^+}{\partial\zeta_k^+}} - \frac{\nu}{4}\overline{\frac{\partial u_i'^-}{\partial\zeta_k^-}\frac{\partial u_i'^-}{\partial\zeta_k^-}}
\end{aligned} \tag{2.4}$$

where $P_r = -\overline{\delta u'_j\delta u'_i}\frac{\partial\delta\overline{u_i}}{\partial r_j} = -\overline{\delta u'_j\delta u'_i}\frac{1}{2}[\Sigma_{ij}(\mathbf{X}+\mathbf{r}) + \Sigma_{ij}(\mathbf{X}-\mathbf{r})]$ and $P_{Xr}^s = -\overline{u'_{Xj}\delta u'_i}\frac{\partial\delta\overline{u_i}}{\partial X_j}$, with $\Sigma_{ij} \equiv \frac{1}{2}(\frac{\partial\overline{u_i}}{\partial X_j} + \frac{\partial\overline{u_j}}{\partial X_i})$, are two-point turbulence production rates. Indeed, being proportional to mean flow gradient terms and to averages of products of fluctuating velocities, they represent linear turbulence fluctuation processes and they exchange energy between $|\boldsymbol{\delta\overline{u}}|^2$ and $\overline{|\boldsymbol{\delta u}'|^2}$ because they appear with opposite signs in equations (2.3) and (2.4) as already noted by Alves Portela *et al.* (2017).

The two-point turbulence production terms P_r and P^s_{Xr} differ. P_r results from the product of the two-point small-scale Reynolds stress $\overline{\delta u'_j \delta u'_i}$ with the two-point half sum of mean strain rates $\frac{1}{2}(\Sigma_{ij}(\mathbf{X}+\mathbf{r}) + \Sigma_{ij}(\mathbf{X}-\mathbf{r}))$ both of which are symmetric in (i,j). On the other hand, P^s_{Xr} results from the product of non-symmetric small/large-scale correlation $\overline{u'_{Xj}\delta u'_i}$ with the two-point gradient $\frac{\partial \delta \overline{u_i}}{\partial X_j}$. To better set the context for the two-point turbulence production rate P^s_{Xr} one needs to consider the evolution equation for the two-point velocity half sum $\boldsymbol{u_X}(\boldsymbol{X},\boldsymbol{r},t)$.

This equation was first obtained by Germano (2007):

$$\frac{\partial \boldsymbol{u_X}}{\partial t} + (\boldsymbol{u_X}.\boldsymbol{\nabla_X})\,\boldsymbol{u_X} + (\boldsymbol{\delta u}.\boldsymbol{\nabla_r})\,\boldsymbol{u_X} = -\boldsymbol{\nabla_X} p_X + \frac{\nu}{2}\boldsymbol{\nabla_X}^2\boldsymbol{u_X} + \frac{\nu}{2}\boldsymbol{\nabla_r}^2\boldsymbol{u_X} \tag{2.5}$$

where $p_X \equiv \frac{p^+ + p^-}{2}$, and note that $\boldsymbol{u_X}$ is incompressible, i.e. $\boldsymbol{\nabla_X}.\boldsymbol{u_X} = \boldsymbol{\nabla_r}.\boldsymbol{u_X} = 0$. An energy equation, also first derived by Germano (2007), is readily obtained by multiplying equation 2.5 with $2\boldsymbol{u_X}$:

$$\frac{\partial |\boldsymbol{u_X}|^2}{\partial t} + \boldsymbol{\nabla_X}.(\boldsymbol{u_X}|\boldsymbol{u_X}|^2) + \boldsymbol{\nabla_r}.(\boldsymbol{\delta u}|\boldsymbol{u_X}|^2) = -2\boldsymbol{\nabla_X}.(\boldsymbol{u_X}P_X) + \frac{\nu}{2}\boldsymbol{\nabla_X}^2|\boldsymbol{u_X}|^2 + \frac{\nu}{2}\boldsymbol{\nabla_r}^2|\boldsymbol{u_X}|^2 - \frac{1}{2}\epsilon^+ - \frac{1}{2}\epsilon^- \tag{2.6}$$

A pair of Reynolds averaged two-point energy equations follows (using $p_X = \overline{p_X} + p'_X$):

$$\begin{aligned}&(\overline{\boldsymbol{u_X}}.\boldsymbol{\nabla_X} + \boldsymbol{\delta\overline{u}}.\boldsymbol{\nabla_r})\,\frac{1}{2}|\overline{\boldsymbol{u_X}}|^2 + P_X + P^l_{Xr} + \frac{\partial}{\partial x_j}(\overline{u_{Xi}}\,\overline{u'_{Xi}u'_{Xj}}) + \frac{\partial}{\partial r_j}(\overline{u_{Xi}}\,\overline{\delta u'_j u'_{Xi}}) \\ &= -\boldsymbol{\nabla_X}.(\overline{\boldsymbol{u_X}}\,\overline{p_X}) + \frac{\nu}{2}\boldsymbol{\nabla_X}^2\frac{1}{2}|\overline{\boldsymbol{u_X}}|^2 + \frac{\nu}{2}\boldsymbol{\nabla_r}^2\frac{1}{2}|\overline{\boldsymbol{u_X}}|^2 - \frac{\nu}{4}\frac{\partial \overline{u}^+_i}{\partial \zeta^+_k}\frac{\partial \overline{u}^+_i}{\partial \zeta^+_k} - \frac{\nu}{4}\frac{\partial \overline{u}^-_i}{\partial \zeta^-_k}\frac{\partial \overline{u}^-_i}{\partial \zeta^-_k}\end{aligned} \tag{2.7}$$

$$\begin{aligned}&(\overline{\boldsymbol{u_X}}.\boldsymbol{\nabla_X} + \boldsymbol{\delta\overline{u}}.\boldsymbol{\nabla_r})\,\frac{1}{2}\overline{|\boldsymbol{u'_X}|^2} - P_X - P^l_{Xr} + \boldsymbol{\nabla_X}.\overline{(\boldsymbol{u_X}'\frac{1}{2}|\boldsymbol{u_X}'|^2)} + \boldsymbol{\nabla_r}.\overline{(\boldsymbol{\delta u}'\frac{1}{2}|\boldsymbol{u_X}'|^2)} \\ &= -\boldsymbol{\nabla_X}.(\overline{\boldsymbol{u_X}'p'_X}) + \frac{\nu}{2}\boldsymbol{\nabla_X}^2\frac{1}{2}\overline{|\boldsymbol{u'_X}|^2} + \frac{\nu}{2}\boldsymbol{\nabla_r}^2\frac{1}{2}\overline{|\boldsymbol{u'_X}|^2} - \frac{\nu}{4}\overline{\frac{\partial u'^+_i}{\partial \zeta^+_k}\frac{\partial u'^+_i}{\partial \zeta^+_k}} - \frac{\nu}{4}\overline{\frac{\partial u'^-_i}{\partial \zeta^-_k}\frac{\partial u'^-_i}{\partial \zeta^-_k}}\end{aligned} \tag{2.8}$$

where $P_X = -\overline{u'_{Xj}u'_{Xi}}\frac{\partial \overline{u_{Xi}}}{\partial X_j} = -\overline{u'_{Xj}u'_{Xi}}\frac{1}{2}[\Sigma_{ij}(\mathbf{X}+\mathbf{r}) + \Sigma_{ij}(\mathbf{X}-\mathbf{r})]$ and $P^l_{Xr} = -\overline{\delta u'_j u'_{Xi}}\frac{\partial \delta \overline{u_i}}{\partial X_j}$. These two-point turbulence production rates represent linear turbulence fluctuation processes and an exchange of energy between $|\overline{\boldsymbol{u_X}}|^2$ and $\overline{|\boldsymbol{u'_X}|^2}$ because they appear with opposite signs in equations (2.7) and (2.8).

Once again, the two-point turbulence production terms P_X and P^l_{Xr} differ. P_X results from the product of the two-point large-scale Reynolds stress $\overline{u'_{Xj}u'_{Xi}}$ with the two-point half sum of mean strain rates $\frac{1}{2}(\Sigma_{ij}(\mathbf{X}+\mathbf{r}) + \Sigma_{ij}(\mathbf{X}-\mathbf{r}))$ both of which are symmetric in (i,j). This is similar to P_r except that the two-point Reynolds stress is now large-scale rather than small-scale because it is defined in terms of the fluctuating velocity half sum rather than half difference. On the other hand, P^l_{Xr} results from the product of non-symmetric small/large-scale correlation $\overline{u'_{Xi}\delta u'_j}$ with the two-point gradient $\frac{\partial \delta \overline{u_i}}{\partial X_j}$, which is similar to P^s_{Xr}. However, the sum of both, i.e. $P_{Xr} \equiv P^s_{Xr} + P^l_{Xr}$, results from the product of a symmetric small/large-scale correlation $\overline{u'_{Xi}\delta u'_j + u'_{Xj}\delta u'_i}$ with $\frac{1}{2}[\Sigma_{ij}(\mathbf{X}+\mathbf{r}) - \Sigma_{ij}(\mathbf{X}-\mathbf{r})]$ and contributes to the linear transfer of energy by total production rate $P_X + P_r + P_{Xr}$ between $\frac{1}{2}|\overline{\boldsymbol{u}}^+|^2 + \frac{1}{2}|\overline{\boldsymbol{u}}^-|^2$ and $\frac{1}{2}\overline{|\boldsymbol{u}'^+|^2} + \frac{1}{2}\overline{|\boldsymbol{u}'^+|^2}$.

3. Interscale turbulent energy transfers

Besides two-point turbulent production terms, the two-point energy equations of the previous section involve important interscale and interspace transport terms. Germano (2007) interpreted his equations 2.5 and 2.6 in the context of large eddy simulations (LES). He showed that the term $(\boldsymbol{\delta u}.\boldsymbol{\nabla_r})\,\boldsymbol{u_X}$ in equation 2.5 can be interpreted as the gradient of a subgrid stress. This term gives rise to the term $\boldsymbol{\nabla_r}.(\boldsymbol{\delta u}|\boldsymbol{u_X}|^2)$ in equation 2.6 which is therefore an energy transfer rate between large-scale velocities (velocity half sum) and small-scale velocities (velocity half difference). Germano (2007) also derived the kinematic equation

$$\boldsymbol{\nabla_r}.(\boldsymbol{\delta u}|\boldsymbol{u_X}|^2) + \boldsymbol{\nabla_r}.(\boldsymbol{\delta u}|\boldsymbol{\delta u}|^2) = 2\boldsymbol{\nabla_X}.(\boldsymbol{\delta u}(\boldsymbol{\delta u}\cdot\boldsymbol{u_X})) \tag{3.1}$$

which relates $\boldsymbol{\nabla_r}.(\boldsymbol{\delta u}|\boldsymbol{u_X}|^2)$ to $\boldsymbol{\nabla_r}.(\boldsymbol{\delta u}|\boldsymbol{\delta u}|^2)$ in equation 2.2 where $\boldsymbol{\nabla_r}.(\boldsymbol{\delta u}|\boldsymbol{\delta u}|^2)$ accounts for non-linear interscale energy transfer and the turbulence cascade, e.g. see Chen & Vassilicos (2022).

It must be stressed, however, that the term $\boldsymbol{\nabla_r}.(\boldsymbol{\delta u}|\boldsymbol{\delta u}|^2)$ in equation 2.2 does not only include non-linear interscale transfer responsible for the turbulence cascade, it also includes two-point turbulence production and interscale energy transfer by mean flow differences. Indeed, it gives rise in equation 2.4 to the two-point turbulence production rate P_r, to the linear average interscale turbulent energy transfer rate by mean flow differences $\boldsymbol{\delta\overline{u}}.\boldsymbol{\nabla_r}\overline{|\boldsymbol{\delta u'}|^2}$ and to the non-linear average interscale turbulent energy transfer rate $\boldsymbol{\nabla_r}.(\overline{\boldsymbol{\delta u'}|\boldsymbol{\delta u'}|^2})$ relating to the turbulence cascade. The other terms in the energy equation 2.4 arise from the pressure gradient, the viscous terms and the advection of small-scale velocity $\boldsymbol{\delta u}$ by the large-scale velocity $\boldsymbol{u_X}$ in equation 2.1. In particular, this advection term gives rise to P^s_{Xr} and to the interspace turbulent transport rate of smaller-scale turbulence energy, i.e. $\boldsymbol{\nabla_X}.(\overline{\boldsymbol{u_X}'|\boldsymbol{\delta u'}|^2})$.

Similar observations can be made for the large-scale energy equations 2.6 and 2.8 where $\boldsymbol{\nabla_r}.(\boldsymbol{\delta u}|\boldsymbol{u_X}|^2)$ in 2.6 gives rise in 2.8 to the two-point production rate P^l_{Xr} (not P_X), to the linear average turbulent energy transfer rate by mean flow differences $\boldsymbol{\delta\overline{u}}.\boldsymbol{\nabla_r}\overline{|\boldsymbol{u'_X}|^2}$ and to the fully non-linear average turbulent energy transfer rate $\boldsymbol{\nabla_r}.(\overline{\boldsymbol{\delta u'}|\boldsymbol{u'_X}|^2})$. The other terms in the energy equation 2.8 arise from the pressure gradient, the viscous terms and the self-advection of large-scale velocity $\boldsymbol{u_X}$ in equation 2.5. In particular, this self-advection term gives rise to P_X (not P^l_{Xr}) and to the interspace turbulent transport rate of larger-scale turbulence energy , i.e. $\boldsymbol{\nabla_X}.(\overline{\boldsymbol{u_X}'|\boldsymbol{u_X}'|^2})$

Returning to the two-point turbulence production terms, P_r and P^s_{Xr} appear in the small-scale energy equation 2.4 whereas P_X and P^l_{Xr} appear in the large-scale energy equation 2.8. All four terms vanish if the mean flow is homogeneous but P_r represents turbulence production by mean flow non-homogeneities at small scales whereas P_X represents turbulence production by mean flow non-homogeneities at large scales. It is worth noting that P_X tends to the usual one-point turbulence production rate $-\overline{u'_j u'_i}\Sigma_{ij}$ in the limit $\mathbf{r} \to \mathbf{0}$ ($\boldsymbol{u'}$ is the fluctuating turbulent velocity at one point) whereas P_r tends to zero in that limit. P^l_{Xr} and P^s_{Xr} also tend to zero in that limit but they represent turbulence production by mean flow non-homogeneities that is cross-scale as they involve correlations between the fluctuating velocity half differences and fluctuating velocity half sums. The hypothesis that large and small scales may be uncorrelated leads to the suggestion that P^l_{Xr} and P^s_{Xr} may be increasingly negligible for decreasing $|\mathbf{r}|$, as indeed found for P^s_{Xr} in the intermediate layer of fully developed turbulent channel flow by Apostolidis *et al.* (2023).

Applying Reynolds averaging to the kinematic identity 3.1 we obtain

$$
\begin{aligned}
&\boldsymbol{\nabla_r}.(\overline{\boldsymbol{\delta u}}|\overline{\boldsymbol{\delta u}}|^2) + \boldsymbol{\nabla_r}.(\overline{\boldsymbol{\delta u}}\,\overline{|\boldsymbol{\delta u}'|^2}) + \boldsymbol{\nabla_r}.(\overline{\boldsymbol{\delta u}'|\boldsymbol{\delta u}'|^2}) + 2\boldsymbol{\nabla_r}.(\overline{\boldsymbol{\delta u}'(\boldsymbol{\delta u}'\overline{\boldsymbol{\delta u}})}) \\
&+ \boldsymbol{\nabla_r}.(\overline{\boldsymbol{\delta u}}|\overline{\boldsymbol{u_X}}|^2) + \boldsymbol{\nabla_r}.(\overline{\boldsymbol{\delta u}}\,\overline{|\boldsymbol{u_X}'|^2}) + \boldsymbol{\nabla_r}.(\overline{\boldsymbol{\delta u}'|\boldsymbol{u_X}'|^2}) - 2P^l_{Xr} \\
&= 2\boldsymbol{\nabla_X}.(\overline{\boldsymbol{\delta u}}(\overline{\boldsymbol{\delta u}}.\overline{\boldsymbol{u_X}})) + 2\boldsymbol{\nabla_X}.(\overline{\overline{\boldsymbol{\delta u}}(\boldsymbol{\delta u}'.\boldsymbol{u}'_{\boldsymbol{X}})}) \\
&+ 2\boldsymbol{\nabla_X}.(\overline{\boldsymbol{\delta u}'(\boldsymbol{\delta u}'.\boldsymbol{u}'_{\boldsymbol{X}})}) + 2\boldsymbol{\nabla_X}.(\overline{\boldsymbol{\delta u}'(\overline{\boldsymbol{\delta u}}.\boldsymbol{u}'_{\boldsymbol{X}})}) - 2P_r
\end{aligned}
\tag{3.2}
$$

which demonstrates that, in general, the average interscale turbulent energy transfer rate $\boldsymbol{\nabla_r}.(\overline{\boldsymbol{\delta u}'|\boldsymbol{\delta u}'|^2})$ reflecting the turbulence cascade does not trivially relate with the average turbulent energy transfer $\boldsymbol{\nabla_r}.(\overline{\boldsymbol{\delta u}'|\boldsymbol{u_X}'|^2})$ reflecting work by subgrid stresses (see Germano (2007)).

A notable exception is statistically homogeneous turbulence where $\overline{\boldsymbol{\delta u}} = \mathbf{0}$, $P_r = 0$, $P^l_{Xr} = 0$ and derivatives with respect to $\mathbf{X}$ of third order fluctuating velocity statistics such as $\boldsymbol{\nabla_X}.(\overline{\boldsymbol{\delta u}'(\boldsymbol{\delta u}'.\boldsymbol{u}'_{\boldsymbol{X}})})$ vanish (we cannot assume that $\overline{\boldsymbol{u_X}}.\boldsymbol{\nabla_X}\overline{|\boldsymbol{\delta u}'|^2}$ vanishes), in which case 3.2 reduces to

$$\boldsymbol{\nabla_r}.\overline{\boldsymbol{\delta u}'|\boldsymbol{u}'_{\boldsymbol{X}}|^2} = -\boldsymbol{\nabla_r}.\overline{\boldsymbol{\delta u}'|\boldsymbol{\delta u}'|^2}. \tag{3.3}$$

Under such statistical homogeneity conditions (note that the terms involving pressure fluctuations in equations 2.4 and 2.8 are derivatives with respect to $\mathbf{X}$ of third order fluctuating velocity statistics given the Poisson equation relating pressure and velocities), and by considering scales $|\mathbf{r}|$ large enough to neglect viscous diffusion, fluctuating energy equations 2.4 and 2.8 become, respectively,

$$\overline{\boldsymbol{u_X}}.\boldsymbol{\nabla_X}\overline{|\boldsymbol{\delta u}'|^2} + \boldsymbol{\nabla_r}.(\overline{\boldsymbol{\delta u}'|\boldsymbol{\delta u}'|^2}) \approx -\overline{\epsilon'} \tag{3.4}$$

and

$$\overline{\boldsymbol{u_X}}.\boldsymbol{\nabla_X}\overline{|\boldsymbol{u}'_{\boldsymbol{X}}|^2} + \boldsymbol{\nabla_r}.(\overline{\boldsymbol{\delta u}'|\boldsymbol{u_X}'|^2}) \approx -\overline{\epsilon'} \tag{3.5}$$

where $\overline{\epsilon'}$ is the average turbulence dissipation rate. Kolmogorov's small-scale stationarity hypothesis adapted to these equations states that $\overline{\boldsymbol{u_X}}.\boldsymbol{\nabla_X}\overline{|\boldsymbol{\delta u}'|^2}$ is much smaller in magnitude than $\overline{\epsilon'}$ at small enough scales $|\mathbf{r}|$. With this hypothesis it follows that

$$\boldsymbol{\nabla_r}.\overline{\boldsymbol{\delta u}'|\boldsymbol{\delta u}'|^2} \approx -\overline{\epsilon'}, \tag{3.6}$$

$$\boldsymbol{\nabla_r}.\overline{\boldsymbol{\delta u}'|\boldsymbol{u}'_{\boldsymbol{X}}|^2} \approx \overline{\epsilon'} \tag{3.7}$$

and

$$\overline{\boldsymbol{u_X}}.\boldsymbol{\nabla_X}\overline{|\boldsymbol{u}'_{\boldsymbol{X}}|^2} \approx -2\overline{\epsilon'} \tag{3.8}$$

in an intermediate range of scales large enough to neglect viscous diffusion and small enough to neglect small-scale non-stationarity. Relation 3.6 is Kolmogorov's scale-by-scale equilibrium and relation 3.7 was first derived by Germano (2007). (Hosokawa (2007) assumed isotropy and derived the equivalent of 3.7 for homogeneous isotropic turbulence).

Turbulence is rarely homogeneous. Therefore, the natural question to ask is whether energy transfer balances which may be different from but nevertheless in the same spirit as 3.6 and 3.7 exist in non-homogeneous turbulence. And if they do, how different are they and what determines the difference?

Various different classes of non-homogeneity exist. Apostolidis *et al.* (2023) developed a scale-by-scale turbulent kinetic energy balance theory for the intermediate layer of fully developed turbulent channel flow where interspace turbulent transport rate and two-point pressure-velocity transport are negligible but small-scale production is not. A theory of scale-by-scale turbulent kinetic energy for non-homogeneous turbulence was recently proposed by Chen & Vassilicos (2022) who's approach allowed them to treat equation 2.4 when small-scale interspace turbulent transport and spatial gradients of two-point pressure-velocity correlations are not negligible. In the present paper we study the turbulent flow under the rotating blades in a baffled container (mixer) where the baffles break the rotation in the flow and enhance turbulence. We start by assessing two-point production to determine whether we need to take it into account when applying the theory of Chen & Vassilicos (2022) to equation 2.4. Even if P_r and P^s_{Xr} are negligible, large-scale two-point production is necessarily present at some scales if one-point production is present in the flow.

In the following section we present our experiment and the Particle Image Velocimetry used to make the measurements which we use in subsequent sections to estimate various terms in equations 2.4 and 2.8.

4. Experimental measurements

4.1. *Description of the mixer and experimental configurations*

Experiments are performed with water in the same octagonal shaped, acrylic tank used in (Steiros *et al.* (2017*a*), Steiros *et al.* (2017*b*)). The impeller has a radial four-bladed flat blade turbine, mounted on a stainless steel shaft at the tank's mid-height. The impellers are driven by a stepper motor (Motion Control Products, UK) in microstepping mode (25, 000 steps per rotation), to ensure smooth movement, which is controlled by a function generator (33600A, Agilent, US). The rotation speed and torque signal are measured with the Magtrol torquemeter TS 106/011. The dimensions of the mixer are presented in figure 2 where $D_T = H = 45cm$, $C = H/2$ and $D \approx D_T/2$.

Baffles (vertical bars on the sides of the tank) are used to break the rotation of the flow (figure 3). These baffles are designed based on the prescriptions of Nagata (1975) for close to fully baffled conditions which maximize power consumption and minimize rotation. For a circular tank, this condition is achieved with four baffles of width around $0.12D_T$ where D_T is the tank diameter (see D_T in figure 2). Therefore, four baffles of mixer tank height and 58mm width are used.

To test the robustness of our results we run experiments with two different types of blade geometry which stimulate the turbulence differently: rectangular blades of $44mm \times 99mm$ size (figure 4a) and fractal-like/multiscale blades (figure 4b) of the exact same frontal area $44 \times 99mm^2$ but much longer perimeter. This blade difference affects turbulence properties substantially as the resulting turbulence dissipation rate differs by 30% to 40% at equal rotation speed (see table 3). We use here the two-iteration 'fractal2' blade described in Steiros *et al.* (2017*b*) and shown in figure 4b. Each one of the two types of blade is tested with two different rotor speeds. We therefore conduct experiments in four different configurations. In all cases, the water is filled to the top of the sealed container to minimise the presence of air bubbles in the water.

4.2. *Particle Image Velocimetry settings*

We use 2D2C PIV in the vertical (x, z) plane indicated in figure 5. This figure also shows the field of view which is aligned with that vertical plane and has its centre offset by only 3mm +/-1mm in the y direction from the centreline.

The PIV set up is composed of a camera, a laser, a set of lenses and mirrors to shape the laser beam into a thin light sheet and a Lavision PTU synchronisation unit and a recording computer with Davis 10 from Lavision.

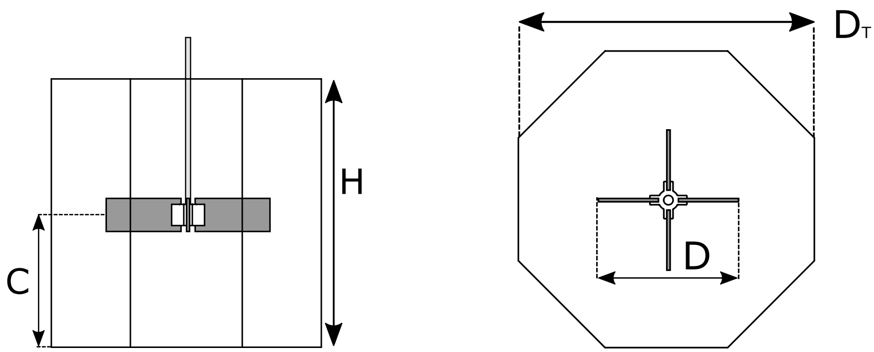

(a) (b)

Figure 2: Mixer dimensions. Figures modified from Steiros *et al.* (2017*b*)

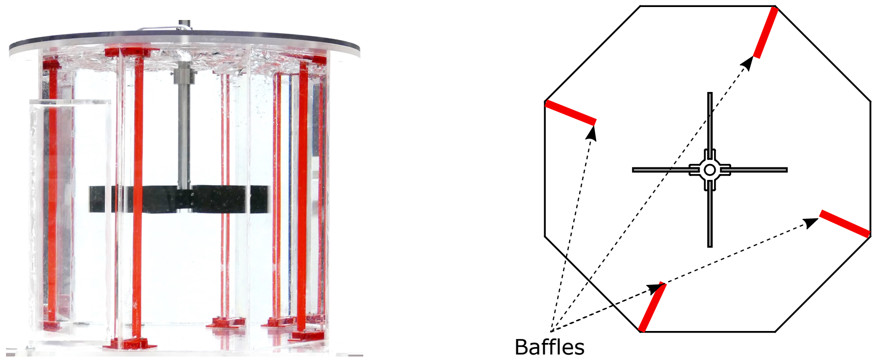

(a) Mixing tank with baffles (b) Top view of baffles

Figure 3: Mixer baffles

(a) Rectangular blade (b) Fractal-like blade

Figure 4: Mixer blades

4.2.1. *Camera*

The camera used is the Phantom v2640 with full sensor image ($2048px \times 1952px$). A Nikon macro Nikkor 200mm lens is used with f#8. The extremity of the lens is at 93 mm from the glass. The field of view size is $C_1 \times C_2 \approx 27mm \times 28mm$ (see figure 5) with a magnification factor of $14.1\mu m/px$.

The acquisition is done by packets of five time-resolved images. The packet acquisition frequency is 6Hz to ensure decorrelation between successive packets. The acquisition frequency for the five images within each packet varies from 1.25kHz to 3kHz depending on type of blade and rotor speed. This parameter is specifically set for each configuration to ensure a turbulent fluctuation displacement between two frames of around 5px (corresponding

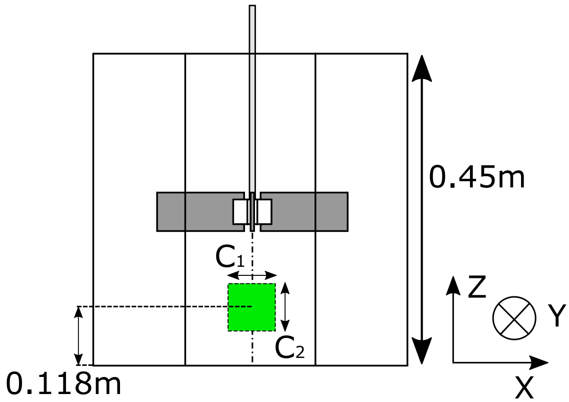

Figure 5: Measurement plane location

to about 1 standard deviation) and maximum 10px (observed with samples during the experiments).

4.2.2. *Laser, mirrors and lenses*

The laser used is the Blizz 30W high speed frequency laser from InnoLas. The laser is optimized at 40kHz with $750\mu J/pulse$ at $532nm$ wavelength and $M^2 < 1.3$. For the experiments it was set to around $500\mu J/pulse$ because of the smaller frequency used. The laser frequency is set according to the camera time-resolved recording frequency. The focal lengths of the spherical and the cylindrical lenses are +800mm and -80mm respectively (beam-waist set in the centre of field of view). The laser sheet height obtained is around 60mm and its width is 0.6mm at the waist (which is close to the centerline of the mixer) with a Rayleigh length of 400 mm. Therefore, the laser sheet's width is constant over the field of view.

4.2.3. *Seeding*

Mono-disperse polystyrene particles Spherotech of diameter $5.33\mu m$ are used. They maximise the concentration in the flow and lead to enough particles within each interrogation window. The background noise is around 30 counts. There are on average about 10 particles per interrogation window of $32px \times 32px$ if a threshold of 50 counts is used to select most particles. This is consistent with the criteria of Keane & Adrian (1991). Among these particles, there is on average 6.5 particles higher than 100 counts per interrogation window.

4.2.4. *Processing*

The calibration is done with LaVision 058-5 plate. The PIV processing is done with the Matpiv toolbox modified at LMFL. It is a classical multigrid and multipass cross-correlation algorithm (Willert & Gharib (1991), Soria (1996)). Here four passes are used, starting with $64px \times 64px$ then, $48px \times 48px$ and finishing with two $32px \times 32px$ passes. Before the final pass, image deformation is used to improve the results (Scarano (2001), Lecordier & Trinité (2004)). An overlap between IW of 62% is used, leading to vector spacing of about 0.17mm. The final grid has then 159 points in the horizontal direction and 167 in the vertical one.

4.3. *Description of the experimental measurements*

4.3.1. *PIV resolution*

The PIV resolution of the experiment (i.e. interrogation window size) is presented in table 1. In terms of the Kolmogorov length $\eta \equiv (\nu^3/\langle\overline{\epsilon'}\rangle)^{1/4}$, where the angular brackets signify a

	F (Hz)	Magnification (microm/px)	Window size (mm)	Window size/ η
Rectangular blades	1	14	0.45	4.1
Rectangular blades	1.5	14	0.45	5.1
Fractal blades	1	14	0.45	3.4
Fractal blades	1.5	14	0.45	4.4

Table 1: PIV resolution

space-average over the PIV field of view, the resolution is between 3.4η and 5.1η depending on configuration. For those configurations where the interrogation window size is higher than 3η the turbulence dissipation rate might be underestimated when denoised properly (Foucaut *et al.* (2021)). However, this underestimation remains acceptable for interrogation window size smaller than 5η where less than 30 % of uncertainty (filtering effect) is expected according to Laizet *et al.* (2015) and Lavoie *et al.* (2007).

4.3.2. *Statistical convergence*

For each configuration, 150 000 velocity fields are recorded in time including 50 000 fully uncorrelated velocity field samples for convergence. Averaging over time is not sufficient for convergence and we therefore also apply averaging over space which greatly improves it. It corresponds to $150000 \times 164 \times 78 \approx 1.9 \times 10^9$ points for one-point statistics where 164×78 is the number of points associated with the vector spacing. For two-point statistics, some spatial points are not available depending on the separation vector size and direction. For zero separation vector, $150000 \times 164 \times 78 \approx 1.9 \times 10^9$ points are available for convergence but for the largest separation vector in r_x direction there are only $150000 \times 164 \approx 2.4 \times 10^7$ points available and in r_z direction only $150000 \times 78 \approx 1.2 \times 10^7$ are available.

The most important results in this paper are reported with error bars quantifying convergence and computed with a bootstrapping method. The central limit theorem is applied to averages over sub-groups of samples of the quantity of interest. For each quantity, 600 sub-groups containing 83 time steps with at least 159 spatial points are used for the computation of an error bar. This method is robust and provides accurate estimations without having to define the number of independent points. The resulting error bars are also representative of the convergence of third order two-point statistics plotted here without error bars as the number of points used is the same.

4.3.3. *Peak-locking*

When a particle is too small, its correlation peak position fit results are biased towards integer values. Therefore, the displacement between two images is more likely to be an integer number of pixels. This peak-locking error (as it is called, Raffel *et al.* (2018)) is systematic (bias error) and is therefore visible on the velocity probability distribution functions (sine modulation) but does not usually impact mean quantities of turbulent flow if enough dynamic is used (here high dynamic is selected of about 5px for one standard deviation, see Christensen (2004)). Peak-locking can be reduced by increasing particles diffraction spot using camera lens aperture F#. However, an increased F# reduces the brightness of the particles and therefore the number of visible particles. In this experiment, F#8 is used as a compromise and some peak locking is still visible. The impact on the results is analyzed in appendix A.3 where we show that energy spectra and averages of two-point velocity quantities such as the interscale turbulent energy transfer rate are unaffected by peak-locking.

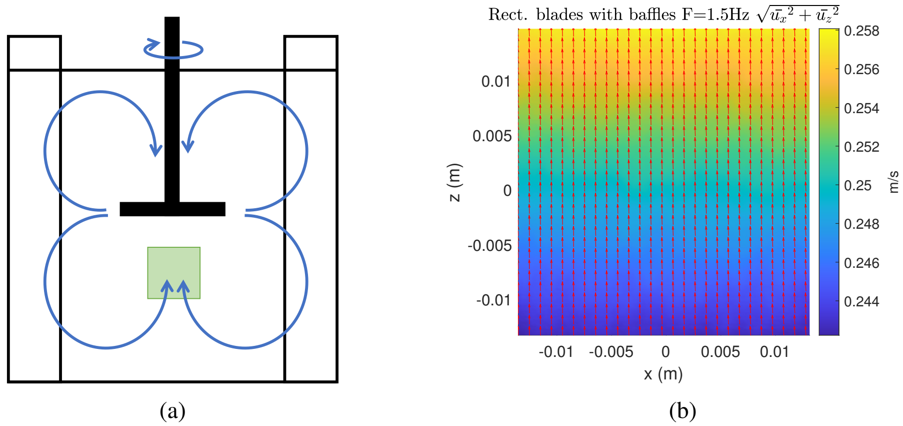

Figure 6: (a): Schematic of mean flow in a mixer with baffles (Nagata (1975)). (b): Mean flow measurement within the measurement plane shown as a green square in (a).

4.3.4. *Defining parameters*

The defining parameters of the experiment are presented in table 2. The rotation frequency F is either 1Hz or 1.5Hz. The global Reynolds number is $Re = \frac{2\pi F R^2}{\nu}$. where $R = D/2 \approx 11.25cm$ is an estimate of the rotor radius. Re is large, higher than 8.10^4, and the flow is therefore turbulent.

The Rossby number is estimated as $Ro = \frac{U}{2\Omega R}$ where U (following Baroud *et al.* (2002)) is the maximum fluctuating velocity in all our samples, R stands in as an estimate of the integral length scale of the turbulence and $\Omega = 2\pi F$. Our values of Ro range between 10^{-1} and 1 and are therefore intermediate between fast rotating and non-rotating turbulence. However, the rotor rotation speed Ω is not representative of flow rotation because the baffles break the flow rotation as explained in Nagata (1975). Therefore, the Rossby number is probably severely underestimated and the rotation is not expected to affect significantly the turbulence behavior in our experiment.

4.3.5. *Basic turbulent flow properties*

The main turbulent parameters are presented in table 3. They include the turbulence dissipation rate $\langle\overline{\epsilon'}\rangle$ averaged over time (overbar) and over space in our field of view (brackets), the resulting Kolmogorov length-scale η (computed with $\langle\overline{\epsilon'}\rangle$) and the Taylor length λ. These parameters are provided as reference and are used in the paper to non-dimensionalise results.

The Taylor length-based Reynolds number Re_λ (see discussion on its estimation in Appendix A.2) is higher than 480 in all four configurations. All the four flows that we study are therefore highly turbulent.

In figure 6b we plot the mean flow velocity for one of our four configurations but the plot is representative of all four configurations. The mean flow velocity is oriented vertically from bottom to top and is not negligible in magnitude. Within our field of view, it is horizontaly uniform and accelerates by about 7% from bottom to top. These observations are consistent with the overall mean flow structure identified by Nagata (1975) and shown in figure 6a.

4.3.6. *2D2C truncations and estimates of 3D3C statistics*

The various terms in the equations of the previous sections require three-component (3C) velocity fields in three-dimensional (3D) space to be calculated. However, our measurements are performed with 2D2C PIV. We can therefore only calculate 2D2C truncations of 3D3C

	$F(Hz)$	Re	vel rms (m/s)	Ro	Mean torque (N.m)
Rectangular blades	1	9.8×10^4	1.0×10^{-1}	3.6×10^{-1}	5.3×10^{-1}
Rectangular blades	1.5	1.3×10^5	1.6×10^{-1}	4.0×10^{-1}	1.1
Fractal blades	1	8.6×10^4	9.1×10^{-2}	3.2×10^{-1}	4.1×10^{-1}
Fractal blades	1.5	1.2×10^5	1.4×10^{-1}	3.4×10^{-1}	8.1×10^{-1}

Table 2: Main parameters of the experiment: vel rms (m/s) stands for $\sqrt{\overline{< u_x'^2 >} + \overline{< u_z'^2 >}}$

	$F(Hz)$	$\langle\overline{\epsilon'}\rangle$ (m^2/s^3)	$\eta(m)$	$\lambda(m)$	Re_λ
Rectangular blades	1	3.6×10^{-3}	1.1×10^{-4}	4.1×10^{-3}	5.1×10^2
Rectangular blades	1.5	1.2×10^{-2}	8.8×10^{-5}	3.7×10^{-3}	6.5×10^2
Fractal blades	1	2.4×10^{-3}	1.3×10^{-4}	4.9×10^{-3}	4.8×10^2
Fractal blades	1.5	8.2×10^{-3}	1.0×10^{-4}	4.1×10^{-3}	5.8×10^2

Table 3: Main turbulence parameters. The Kolmogorov length scale is calculated as $\eta \equiv (\nu^3/\langle\overline{\epsilon'}\rangle)^{1/4}$. The Taylor length and the Reynolds number Re_λ are calculated as in Appendix A.2

statistics and in a few cases (section 5 and section 6) we estimate 2D2C surrogates of 3D3C terms.

5. Two-point turbulence production rates

We start our data analysis with an assessment of two-point turbulence production rates. We define our coordinate system such that components $i = 1$, $i = 2$ and $i = 3$ correspond to the x, y and z directions respectively and therefore $(r_1, r_2, r_3) = (r_x, r_y, r_z)$ and $(X_1, X_2, X_3) = (X_x, X_y, X_z)$. The sums defining $P_r = -\overline{\delta u'_j \delta u'_i}\frac{\partial \overline{\delta u_i}}{\partial r_j}$, $P^s_{Xr} = -\overline{u'_{Xj}\delta u'_i}\frac{\partial \overline{\delta u_i}}{\partial X_j}$, $P_X = -\overline{u'_{Xj}u'_{Xi}}\frac{\partial \overline{u_{Xi}}}{\partial X_j}$ and $P^l_{Xr} = -\overline{\delta u'_j u'_{Xi}}\frac{\partial \overline{\delta u_i}}{\partial X_j}$ are sums of nine terms of which our 2D2C PIV has access to four. Our data therefore allow only truncations to be calculated directly and we start with the truncation of P_r:

$$\widetilde{P_r} = \overline{\delta u'_x \delta u'_x}\frac{\partial \overline{\delta u_x}}{\partial r_x} + \overline{\delta u'_x \delta u'_z}\frac{\partial \overline{\delta u_z}}{\partial r_x} + \overline{\delta u'_z \delta u'_x}\frac{\partial \overline{\delta u_x}}{\partial r_z} + \overline{\delta u'_z \delta u'_z}\frac{\partial \overline{\delta u_z}}{\partial r_z} \tag{5.1}$$

with $\overline{\delta u'_y \delta u'_y}\frac{\partial \overline{\delta u_y}}{\partial r_y} + \overline{\delta u'_x \delta u'_y}\frac{\partial \overline{\delta u_y}}{\partial r_x} + \overline{\delta u'_x \delta u'_y}\frac{\partial \overline{\delta u_x}}{\partial r_y} + \overline{\delta u'_z \delta u'_y}\frac{\partial \overline{\delta u_y}}{\partial r_z} + \overline{\delta u'_z \delta u'_y}\frac{\partial \overline{\delta u_z}}{\partial r_y}$ being the difference between $\widetilde{P_r}$ and P_r. We know from our measurements and from Nagata (1975) that the mean flow is vertical in our field of view which is small and very close to the centreline of the tank. Hence, we can readily neglect all the terms making the difference between $\widetilde{P_r}$ and P_r except $\overline{\delta u'_z \delta u'_y}\frac{\partial \overline{\delta u_z}}{\partial r_y}$. Making the assumption that $\overline{\delta u'_z \delta u'_y}\frac{\partial \overline{\delta u_z}}{\partial r_y} \approx \overline{\delta u'_z \delta u'_x}\frac{\partial \overline{\delta u_z}}{\partial r_x}$ we form the following surrogate estimate of P_r:

$$\widetilde{\widetilde{P_r}} = \overline{\delta u'_x \delta u'_x}\frac{\partial \overline{\delta u_x}}{\partial r_x} + 2\overline{\delta u'_x \delta u'_z}\frac{\partial \overline{\delta u_z}}{\partial r_x} + \overline{\delta u'_z \delta u'_x}\frac{\partial \overline{\delta u_x}}{\partial r_z} + \overline{\delta u'_z \delta u'_z}\frac{\partial \overline{\delta u_z}}{\partial r_z}. \tag{5.2}$$

Similarly, we have the following truncations and surrogate estimates for the other three two-point turbulence production rates:

$$\widetilde{P^s_{Xr}} = \overline{u'_{Xx}\delta u'_x}\frac{\partial\overline{\delta u_x}}{\partial X_x} + \overline{u'_{Xx}\delta u'_z}\frac{\partial\overline{\delta u_z}}{\partial X_x} + \overline{u'_{Xz}\delta u'_x}\frac{\partial\overline{\delta u_x}}{\partial X_z} + \overline{u'_{Xz}\delta u'_z}\frac{\partial\overline{\delta u_z}}{\partial X_z} \tag{5.3}$$

and

$$\widetilde{\widetilde{P^s_{Xr}}} = \overline{u'_{Xx}\delta u'_x}\frac{\partial\overline{\delta u_x}}{\partial X_x} + 2\overline{u'_{Xx}\delta u'_z}\frac{\partial\overline{\delta u_z}}{\partial X_x} + \overline{u'_{Xz}\delta u'_x}\frac{\partial\overline{\delta u_x}}{\partial X_z} + \overline{u'_{Xz}\delta u'_z}\frac{\partial\overline{\delta u_z}}{\partial X_z}; \tag{5.4}$$

$$\widetilde{P_X} = \overline{u'_{Xx}u'_{Xx}}\frac{\partial\overline{u_{Xx}}}{\partial X_x} + \overline{u'_{Xx}u'_{Xz}}\frac{\partial\overline{u_{Xz}}}{\partial X_x} + \overline{u'_{Xz}u'_{Xx}}\frac{\partial\overline{u_{Xx}}}{\partial X_z} + \overline{u'_{Xz}u'_{Xz}}\frac{\partial\overline{u_{Xz}}}{\partial X_z} \tag{5.5}$$

and

$$\widetilde{\widetilde{P_X}} = \overline{u'_{Xx}u'_{Xx}}\frac{\partial\overline{u_{Xx}}}{\partial X_x} + 2\overline{u'_{Xx}u'_{Xz}}\frac{\partial\overline{u_{Xz}}}{\partial X_x} + \overline{u'_{Xz}u'_{Xx}}\frac{\partial\overline{u_{Xx}}}{\partial X_z} + \overline{u'_{Xz}u'_{Xz}}\frac{\partial\overline{u_{Xz}}}{\partial X_z}; \tag{5.6}$$

$$\widetilde{P^l_{Xr}} = \overline{\delta u'_x u'_{Xx}}\frac{\partial\overline{\delta u_x}}{\partial r_x} + \overline{\delta u'_x u'_{Xz}}\frac{\partial\overline{\delta u_z}}{\partial r_x} + \overline{\delta u'_z u'_{Xx}}\frac{\partial\overline{\delta u_x}}{\partial r_z} + \overline{\delta u'_z u'_{Xz}}\frac{\partial\overline{\delta u_z}}{\partial r_z} \tag{5.7}$$

and

$$\widetilde{\widetilde{P^l_{Xr}}} = \overline{\delta u'_x u'_{Xx}}\frac{\partial\overline{\delta u_x}}{\partial r_x} + 2\overline{\delta u'_x u'_{Xz}}\frac{\partial\overline{\delta u_z}}{\partial r_x} + \overline{\delta u'_z u'_{Xx}}\frac{\partial\overline{\delta u_x}}{\partial r_z} + \overline{\delta u'_z u'_{Xz}}\frac{\partial\overline{\delta u_z}}{\partial r_z}. \tag{5.8}$$

We calculate space averages over the field of view of the four truncated and the four surrogate two-point production rates in the eight equations above. In figures 7,8, 9 and 10 we plot, versus $r_1 \equiv r_x$ and $r_3 \equiv r_z$, the four average surrogate two-point production rates $\langle\widetilde{\widetilde{P_r}}\rangle$, $\langle\widetilde{\widetilde{P^l_{Xr}}}\rangle$, $\langle\widetilde{\widetilde{P_X}}\rangle$ and $\langle\widetilde{\widetilde{P^l_{Xr}}}\rangle$ where the brackets signify space-averaging. We plot them normalised by $\frac{\langle\overline{\epsilon'}\rangle}{2}$ where $\epsilon' \equiv \nu\frac{\partial u'_i}{\partial\zeta_j}\frac{\partial u'_i}{\partial\zeta_j}$ is estimated on the basis of our 2D2C PIV data using its axisymmetric formulation (see Appendix A.1 where we also report that we did not find very significant differences in the values of $\langle\overline{\epsilon'}\rangle$ calculated either on the basis of small-scale axisymmetry or on the basis of small-scale isotropy). $\frac{\langle\overline{\epsilon'}\rangle}{2}$ is used to non-dimensionalize results instead of $\langle\overline{\epsilon'}\rangle$ because the turbulence dissipation term in equation 2.4, once averaged in space, is $< \frac{\nu}{4}\overline{\frac{\partial u'^+_i}{\partial\zeta^+_k}\frac{\partial u'^+_i}{\partial\zeta^+_k}} + \frac{\nu}{4}\overline{\frac{\partial u'^-_i}{\partial\zeta^-_k}\frac{\partial u'^-_i}{\partial\zeta^-_k}} > \approx \frac{1}{2} < \overline{\epsilon'} >$.

In the plots in figures 7 and 8, $\langle\widetilde{\widetilde{P_r}}\rangle$ is relatively small and $\langle\widetilde{\widetilde{P^s_{Xr}}}\rangle$ is negligible, irrespective of experimental configuration, for most values of r_x and r_z that our field of view allows us to access. Plots, not shown here for economy of space, of the corresponding truncations $\langle\widetilde{P_r}\rangle$ and $\langle\widetilde{P^s_{Xr}}\rangle$ are very similar. The largest absolute values of $\langle\widetilde{\widetilde{P_r}}\rangle$ are obtained at relatively large scales $r_z = 5\lambda \approx R/5$ with values around $0.15\frac{\langle\overline{\epsilon'}\rangle}{2}$ which is not negligible but still relatively small. These values decrease with decreasing two-point separation lengths as $\langle\widetilde{\widetilde{P_r}}\rangle$ tends to zero when $\boldsymbol{r}$ tends to zero. Furthermore, the increase of $\langle\widetilde{\widetilde{P_r}}\rangle$ with increasing two-point separation is also much smaller than the increase of two-point turbulence production in the intermediate layer of fully developed turbulent channel flow found by Apostolidis *et al.* (2023). We are therefore encouraged to hypothesise that two-point turbulence production by mean flow non-homogeneities at small scales and cross-scale two-point turbulence production are negligible in the small-scale energy equation 2.4 for the present turbulent flows.

Looking at figure 10, we can equally hypothesise that cross-scale two-point production is also negligible in the large-scale energy equation 2.8, and a similar conclusion arises from

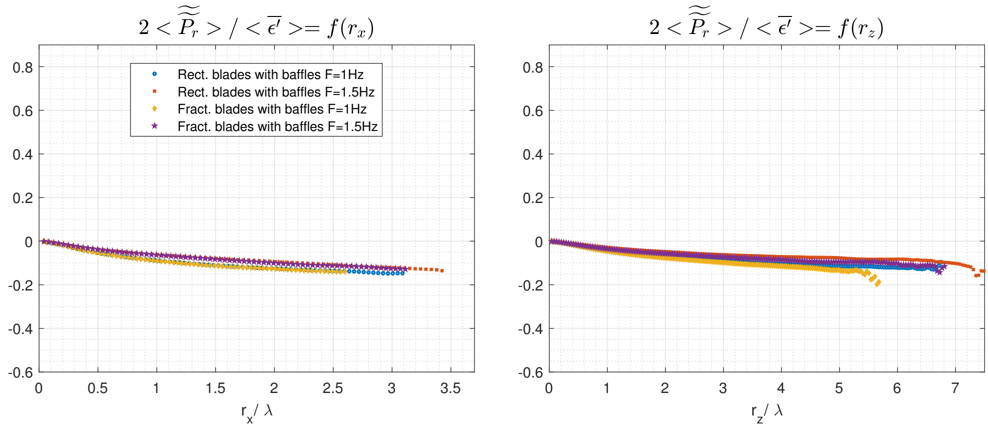

(a) r_x direction (b) r_z direction

Figure 7: Production surrogate defined in equation 5.2 along two radial directions

respective plots of the average surrogate $\langle \widetilde{P^l_{Xr}} \rangle$ (not shown given the very close resemblance with figure 10). However, unlike $\langle \widetilde{\widetilde{\widetilde{P_r}}} \rangle$, $\langle \widetilde{P_r} \rangle$, $\langle \widetilde{\widetilde{\widetilde{P^l_{Xr}}}} \rangle$, $\langle \widetilde{P^l_{Xr}} \rangle$, $\langle \widetilde{\widetilde{\widetilde{P^l_{Xr}}}} \rangle$ and $\langle \widetilde{P^l_{Xr}} \rangle$ which are all close to zero over a wide range of scales r_x and r_z for all four experimental configurations, $\langle \widetilde{\widetilde{P_X}} \rangle$ and $\langle \widetilde{P_X} \rangle$ do not decrease towards 0 with decreasing two-point separation and can even be comparable to $\frac{\langle \overline{\epsilon'} \rangle}{2}$ at the very smallest separations. Figure 9 shows this clearly for $\langle \widetilde{\widetilde{P_X}} \rangle$ and the corresponding plots (not shown here) for $\langle \widetilde{P_X} \rangle$ are qualitatively similar but with different quantitative values. In particular, $\langle \widetilde{\widetilde{P_X}} \rangle$ and $\langle \widetilde{P_X} \rangle$ do not tend to zero as $\mathbf{r}$ tends to 0 in agreement with the point made in section 2 that P_X tends to $-\overline{u'_j u'_i} \Sigma_{ij}$ in the limit $\mathbf{r} \to \mathbf{0}$ and therefore does not tend to zero if there is non-vanishing one-point turbulence production present in the flow. However, the ratios $2\langle \widetilde{\widetilde{P_X}} \rangle / \langle \overline{\epsilon'} \rangle$ and $2\langle \widetilde{P_X} \rangle / \langle \overline{\epsilon'} \rangle$ differ between configurations, and in particular for different types of blade, suggesting that there are non-homogeneity differences between the four configurations considered here. In spite of these differences, $\langle \widetilde{\widetilde{P_X}} \rangle$ and $\langle \widetilde{P_X} \rangle$ are typically negative in all confugurations suggesting that energy is transferred from the fluctuations to the mean.

Overall, our data support the hypothesis that, for the turbulent flows considered here and for scales small enough compared to the flow's large scales, two-point production may be neglected in the small-scale energy equation 2.4 even if P_X cannot be neglected in the large-scale energy equation 2.8. This is not a trivial hypothesis because P_r was found by Apostolidis *et al.* (2023) not to be negligible at scales comparable to and larger than the Taylor length in the intermediate layer of fully developed turbulent channel flow where the turbulence is also non-homogeneous.

6. Small scale linear transport terms

Given the previous section's conclusion which encourages us to neglect two-point production in the small-scale energy equation 2.4 but not in the large-scale energy equation 2.8, we now focus on equation 2.4 and ask whether we can justify simplifying it further by neglecting the linear transport rate $(\overline{\boldsymbol{u}_X}.\boldsymbol{\nabla}_X + \delta\overline{\boldsymbol{u}}.\boldsymbol{\nabla}_r)\, \frac{1}{2}\overline{|\boldsymbol{\delta u'}|^2}$. Once again, with our 2D2C PIV data, we can only consider a truncation and a surrogate estimate. The truncation

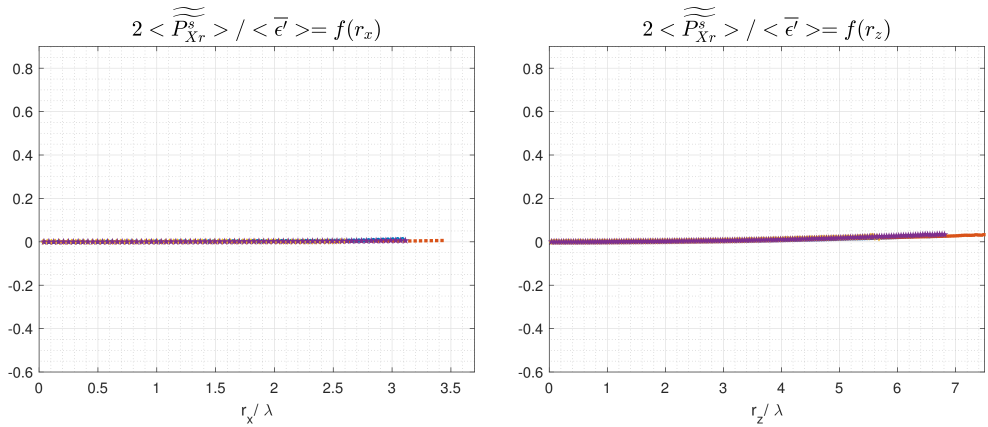

(a) r_x direction

(b) r_z direction

Figure 8: Production surrogate defined in equation 5.4 along two radial directions

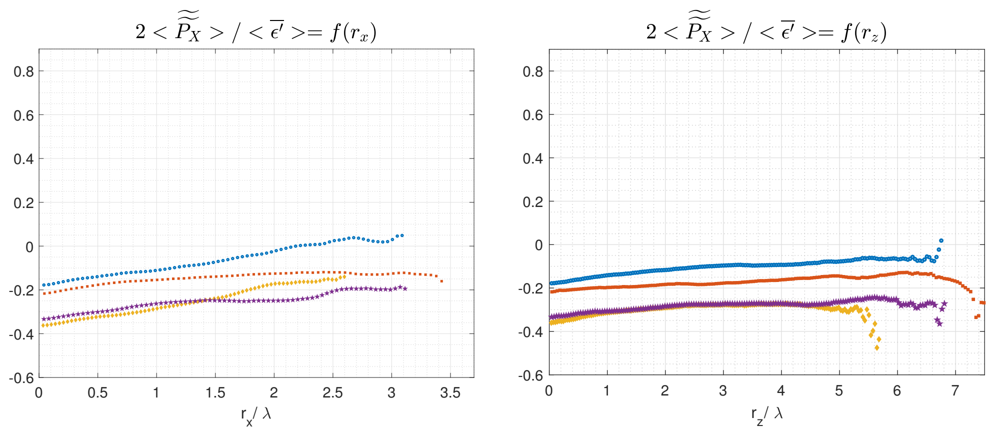

(a) r_x direction

(b) r_z direction

Figure 9: Production surrogate defined in equation 5.6 along two radial directions

is $\left(\overline{u_{Xx}}\frac{\partial}{\partial X_x} + \overline{u_{Xz}}\frac{\partial}{\partial X_z} + \overline{\delta u_x}\frac{\partial}{\partial r_x} + \overline{\delta u_z}\frac{\partial}{\partial r_z}\right)\frac{1}{2}\left(\overline{\delta u_x'^2 + \delta u_z'^2}\right)$ and the surrogate estimate is obtained by making the assumptions $\overline{\delta u_x'^2} = \overline{\delta u_y'^2}$, $\overline{u_{Xx}}\frac{\partial}{\partial X_x}\frac{1}{2}\overline{|\boldsymbol{\delta u'}|^2} = \overline{u_{Xy}}\frac{\partial}{\partial X_y}\frac{1}{2}\overline{|\boldsymbol{\delta u'}|^2}$ and $\overline{\delta u_x}\frac{\partial}{\partial r_x}\frac{1}{2}\overline{|\boldsymbol{\delta u'}|^2} = \overline{\delta u_y}\frac{\partial}{\partial r_y}\frac{1}{2}\overline{|\boldsymbol{\delta u'}|^2}$. Our surrogate estimate of $(\overline{\boldsymbol{u_X}}.\boldsymbol{\nabla_X} + \overline{\boldsymbol{\delta u}}.\boldsymbol{\nabla_r})\frac{1}{2}\overline{|\boldsymbol{\delta u'}|^2}$ is therefore $\left(2\overline{u_{Xx}}\frac{\partial}{\partial X_x} + \overline{u_{Xz}}\frac{\partial}{\partial X_z} + 2\overline{\delta u_x}\frac{\partial}{\partial r_x} + \overline{\delta u_z}\frac{\partial}{\partial r_z}\right)\frac{1}{2}\left(\overline{2\delta u_x'^2 + \delta u_z'^2}\right)$.

We calculate space-averages of the truncation and the surrogate estimate in two parts: i.e. $\langle\left(\overline{u_{Xx}}\frac{\partial}{\partial X_x} + \overline{u_{Xz}}\frac{\partial}{\partial X_z}\right)\frac{1}{2}\left(\overline{\delta u_x'^2 + \delta u_z'^2}\right)\rangle$ and $\langle\left(\overline{\delta u_x}\frac{\partial}{\partial r_x} + \overline{\delta u_z}\frac{\partial}{\partial r_z}\right)\frac{1}{2}\left(\overline{\delta u_x'^2 + \delta u_z'^2}\right)\rangle$ for the truncation, and for the surrogate estimate $\langle\left(2\overline{u_{Xx}}\frac{\partial}{\partial X_x} + \overline{u_{Xz}}\frac{\partial}{\partial X_z}\right)\frac{1}{2}\left(\overline{2\delta u_x'^2 + \delta u_z'^2}\right)\rangle$ and $\langle\left(2\overline{\delta u_x}\frac{\partial}{\partial r_x} + \overline{\delta u_z}\frac{\partial}{\partial r_z}\right)\frac{1}{2}\left(\overline{2\delta u_x'^2 + \delta u_z'^2}\right)\rangle$. Both parts of the space-average truncation and of the space-average surrogate are relatively small compared to $\langle\overline{\epsilon'}\rangle/2$ over a significant range of scales in all four configurations, increasing slowly in magnitude with increasing $|\boldsymbol{r}|$ and reaching at $r_z = 6.8\lambda \approx 0.3R$ a value of $0.23\langle\overline{\epsilon'}\rangle/2$ for the conservative surrogate estimate

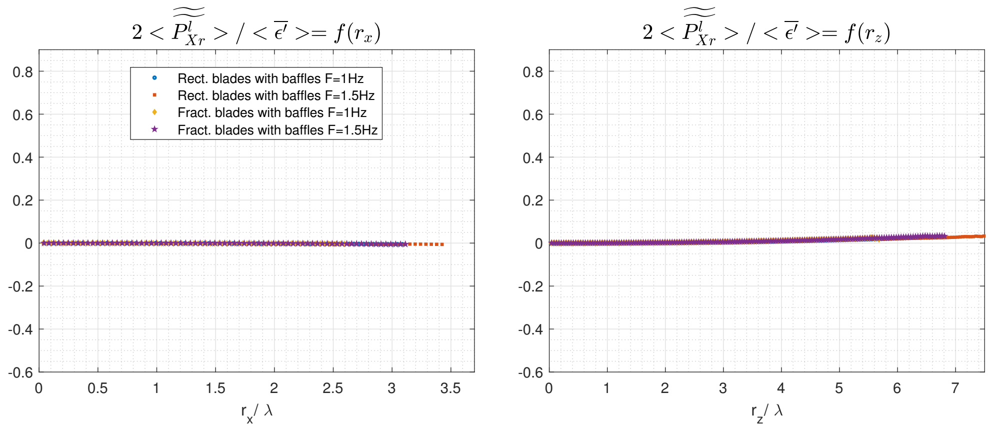

(a) r_x direction (b) r_z direction

Figure 10: Production surrogate defined in equation 5.8 along two radial directions

and of $0.14\langle\overline{\epsilon'}\rangle/2$ for the truncation. In figures 11a, 11b, 12a and 12b we plot the two space-average surrogate parts normalised by $\langle\overline{\epsilon'}\rangle/2$ versus r_x and r_z.

There are therefore grounds to support the additional hypothesis that $(\overline{\boldsymbol{u}_{\boldsymbol{X}}}.\boldsymbol{\nabla}_{\boldsymbol{X}} + \boldsymbol{\delta}\overline{\boldsymbol{u}}.\boldsymbol{\nabla}_{\boldsymbol{r}})\,\frac{1}{2}\overline{|\boldsymbol{\delta u'}|^2}$ might also be neglected from the small-scale energy equation 2.4 at small enough scales. We therefore consider the following simplified form of this equation for the turbulent flow region studied here:

$$\boldsymbol{\nabla}_{\boldsymbol{X}}.(\overline{\boldsymbol{u}_{\boldsymbol{X}}'|\boldsymbol{\delta u'}|^2}) + \boldsymbol{\nabla}_{\boldsymbol{r}}.(\overline{\boldsymbol{\delta u'}|\boldsymbol{\delta u'}|^2}) + 2\boldsymbol{\nabla}_{\boldsymbol{X}}.\overline{(\boldsymbol{\delta u'}\delta p')} \approx \frac{\nu}{2}({\boldsymbol{\nabla}_{\boldsymbol{X}}}^2 + {\boldsymbol{\nabla}_{\boldsymbol{r}}}^2)\overline{|\boldsymbol{\delta u'}|^2} - \frac{1}{2}\left(\overline{\epsilon'^{+}} + \overline{\epsilon'^{-}}\right) \tag{6.1}$$

where $\overline{\epsilon'^{+}}$ and $\overline{\epsilon'^{-}}$ are $\overline{\epsilon'}$ at $\boldsymbol{\zeta}^{+}$ and $\boldsymbol{\zeta}^{-}$ respectively. Note, however, that this additional hypothesis concerning $(\overline{\boldsymbol{u}_{\boldsymbol{X}}}.\boldsymbol{\nabla}_{\boldsymbol{X}} + \boldsymbol{\delta}\overline{\boldsymbol{u}}.\boldsymbol{\nabla}_{\boldsymbol{r}})\,\frac{1}{2}\overline{|\boldsymbol{\delta u'}|^2}$ is in fact not crucial because the conclusions of the following two sections can also be obtained without it (with the only potential exception of the last sentence of subsection 8.4 which may need to be qualified).

It is worth pointing out that a careful look at all figures 7,8, 9 and 10 as well as figure 11a, 11b, 12a and 12b suggests that the approximation 6.1 does not necessarily hold for large enough values of r_x and/or r_z. We chose to normalise r_x and r_z by λ in all these figures for comparison with Apostolidis *et al.* (2023) who found, in a very different non-homogeneous turbulent flow (namely the intermediate region of fully developed turbulent channel flow), that equation 6.1 is not a good approximation at scales comparable to and larger than λ whereas we do assume it to be a good approximation at such scales (if they are not too large) in the flow region of the non-homogeneous turbulent flows considered here.

7. Second order structure functions

We now adopt the approach of Chen & Vassilicos (2022) which is based on inner and outer similarity. In effect, we assume that regions of space exist in the flow where the non-linear and non-local dynamics of the small-scale turbulence are similar at different places within the region. We therefore start with an hypothesis of inner and outer similarity for the second order structure function $\overline{|\boldsymbol{\delta u'}|^2}$, namely

$$\overline{|\boldsymbol{\delta u'}|^2} = V_{O2}^2(\boldsymbol{X})f_{O2}\left(\frac{\boldsymbol{r}}{l_O}\right) \tag{7.1}$$

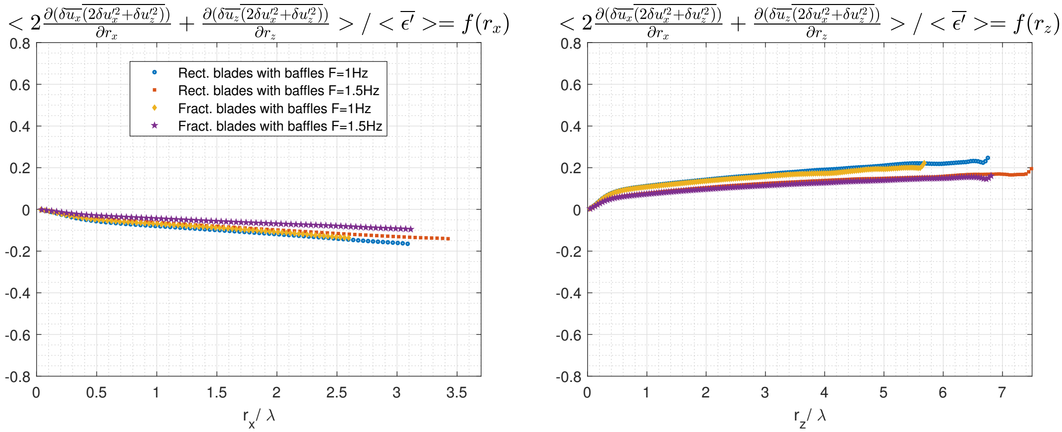

(a) r_x direction (b) r_z direction

Figure 11: Surrogate of rate of linear transport in scales in equation 2.4

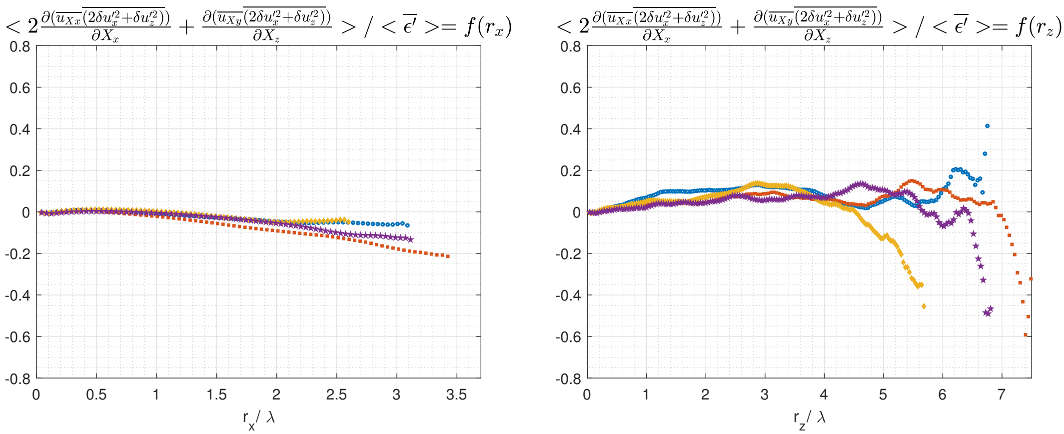

(a) r_x direction (b) r_z direction

Figure 12: Surrogate of rate of linear transport in space in equation 2.4

for $|\boldsymbol{r}| \gg l_I$ and

$$\overline{|\boldsymbol{\delta u'}|^2} = V_{I2}^2(\boldsymbol{X}) f_{I2}\left(\frac{\boldsymbol{r}}{l_I}\right) \tag{7.2}$$

for $|\boldsymbol{r}| \ll l_O$, where the inner length-scale l_I depends on viscosity and is much smaller than the outer length-scale l_O which does not depend on viscosity, i.e. $l_I = l_I(\boldsymbol{X}) \ll l_O = l_O(\boldsymbol{X})$ for large enough Reynolds number. The outer length scale can be thought of as an integral length of the order of the blade size $R = D/2$ and is assumed to be smaller than the extent of the similarity region where (7.1) and (7.2) hold. Statistical homogeneity is a special case of our inner and outer similarity hypotheses where V_{O2}, V_{I2}, l_O and l_I are independent of $\boldsymbol{X}$. In the following section we apply the approach of Chen & Vassilicos (2022) to the small-scale energy balance 6.1.

It is natural to expect the outer characteristic velocity V_{O2} to be independent of viscosity but the inner characteristic velocity V_{I2} to depend on it. The ratios V_{I2}/V_{O2} and l_I/l_O must therefore be functions of a local Reynolds number $Re_O = V_{O2}l_O/\nu$ and we write

$V_{I2}/V_{O2} = g_2(Re_O, \boldsymbol{X})$, $l_I/l_O = g_l(Re_O, \boldsymbol{X})$, these two functions having to tend to zero as Re_O tends to infinity.

The inner and outer similarity forms overlap in the range $l_I \ll |\boldsymbol{r}| \ll l_O$, hence

$$f_{O2}\left(\frac{\boldsymbol{r}}{l_O}\right) = g_2^2(Re_O, \boldsymbol{X}) f_{I2}\left(\frac{\boldsymbol{r}}{l_O} g_l^{-1}\right) \tag{7.3}$$

in this intermediate range. Given that the left hand side of this equation does not depend on Re_O, the derivative with respect to Re_O of the right hand side cancels and we obtain

$$g_l \frac{dg_2^2}{dRe_O} f_{I2}(\boldsymbol{\rho}) = g_2^2 \frac{dg_l}{dRe_O} \rho_j \frac{\partial}{\partial \rho_j} f_{I2}(\boldsymbol{\rho}) \tag{7.4}$$

where there is an implicit sum over $j = 1, 2, 3$ and $\boldsymbol{\rho} = (\rho_1, \rho_2, \rho_3) = \boldsymbol{r}/l_I$. It follows that $\rho_j \frac{\partial}{\partial \rho_j} f_{I2}(\boldsymbol{\rho})$ is proportional to $f_{I2}(\boldsymbol{\rho})$. To solve for f_{I2} we adopt spherical coordinates (ρ, θ, ϕ) for $\boldsymbol{\rho}$, where θ varies from 0 to π and vanishes if $\boldsymbol{\rho}$ is aligned with the y axis and where ϕ varies from 0 to 2π and is equal to 0 or $\pi/2$ if $\boldsymbol{\rho}$ is aligned with the x or the z axis respectively. The proportionality between $\rho_j \frac{\partial}{\partial \rho_j} f_{I2}(\boldsymbol{\rho})$ and $f_{I2}(\boldsymbol{\rho})$ becomes $n f_{I2}(\rho, \theta, \phi) = \rho \frac{\partial}{\partial \rho} f_{I2}(\rho, \theta, \phi)$ in terms of a dimensionless proportionality constant n and the solution to this equation is

$$f_{I2} = \rho^n F(\theta, \phi) \tag{7.5}$$

where F is an unknown function of angles θ and ϕ. Note that 7.5 holds in the intermediate range $l_I \ll |\boldsymbol{r}| \ll l_O$. Returning to 7.3, we get

$$g_2^2(Re_O, \boldsymbol{X}) g_l^{-n}(Re_O, \boldsymbol{X}) = A_1 \tag{7.6}$$

where the dimensionless coefficient A_1 is independent of Re_O and $\boldsymbol{X}$.

At this stage we follow Chen & Vassilicos (2022) and use their hypothesis of inner-outer equivalence for dissipation according to which there is an inner and an outer way to estimate the turbulence dissipation rate: $\overline{\epsilon'} \sim V_{O2}^3/l_O \sim V_{I2}^3/l_I$ where the proportionality coefficients are independent of Re_O but can depend on $\boldsymbol{X}$. We actually derive this hypothesis in subsection 8.3 and our derivation shows clearly that it has nothing to do with Kolmogorov's scale-by-scale equilibrium. At this stage, it provides the additional constraint $g_2^3(Re_O) g_l^{-1}(Re_O) = A_2$ where the coefficient A_2 is independent of Re_O. Combined with this additional constraint, 7.6 yields $n = 2/3$ (and $A_3 = A^{3/2}$, which means that A_2 is also independent of $\boldsymbol{X}$) and therefore

$$\overline{|\boldsymbol{\delta u'}|^2} = C(\overline{\epsilon'} r)^{2/3} F(\theta, \phi) \tag{7.7}$$

in the intermediate range $l_I \ll r = |\boldsymbol{r}| \ll l_O$. Note that, reflecting the dimensionless coefficients in $\overline{\epsilon'} \sim V_{O2}^3/l_O \sim V_{I2}^3/l_I$, the dimensional coefficient C can vary in space but is independent of Reynolds number. This is an obvious difference from Kolmogorov's prediction for the second order structure function which is limited to statistically homogeneous turbulence. This difference highlights the underlying difference in the way that our result 7.7 was obtained compared to Kolmogorov's derivation of his corresponding prediction which resembles 7.7 in the scaling $(\overline{\epsilon'} r)^{2/3}$ but is otherwise different (see Frisch (1995), Pope (2000) and section 2 of Chen & Vassilicos (2022))

We can refine our hypothesis of similarity by replacing it with an hypothesis of isotropic similarity which is an hypothesis of similarity for each component of $\boldsymbol{\delta u'}$, namely

$$\overline{(\delta u_j')^2} = V_{O2}^2(\boldsymbol{X}) f_{O2,j}\left(\frac{\boldsymbol{r}}{l_O}\right) \tag{7.8}$$

for $|\boldsymbol{r}| \gg l_I$ and

$$\overline{(\delta u'_j)^2} = V_{I2}^2(\boldsymbol{X}) f_{I2,j}\left(\frac{\boldsymbol{r}}{l_I}\right) \tag{7.9}$$

for $|\boldsymbol{r}| \ll l_O$ for every $j = 1, 2, 3$. This is not an assumption of isotropy because neither the functions $f_{O2,j}$ nor the functions $f_{I2,j}$ are necessarily the same for different $j = 1, 2, 3$. The argument leading to 7.7 can be repeated for every $j = 1, 2, 3$ yielding

$$\overline{(\delta u'_j)^2} = C_j (\overline{\epsilon'} r)^{2/3} F_j(\theta, \phi) \tag{7.10}$$

in the intermediate range $l_I \ll r = |\boldsymbol{r}| \ll l_O$. The dimensionless coefficient C_j may vary with j and with $\boldsymbol{X}$ and the dimensionless function F_j, which is independent of $\boldsymbol{X}$ and of $r \equiv |\boldsymbol{r}|$, may also vary with j. The determination of the inner length scale l_I requires the small-scale energy balance 6.1. This is done in section 8. We complete the present section by confronting prediction 7.10 with our PIV data. This prediction is similar to Kolmogorov's prediction for second order structure functions but it was derived without the homogeneity assumption required by Kolmogorov's theory and without Kolmogorov's scale-by-scale equilibrium which forms the physical basis of Kolmogorov's dimensional analysis.

7.1. *Second order structure function measurements*

We compute the normalised structure functions $\langle \overline{(\delta u'_j)^2} / \overline{\epsilon'}^{2/3} \rangle$ for $j = 1$ (velocity fluctuations along the x-axis) and $j = 3$ (velocity fluctuations along the z-axis) by averaging over time, i.e. over our 150, 000 samples (which correspond to 50, 000 uncorrelated samples) and also averaging over $\boldsymbol{X}$, i.e. over the planar space of our field of view. The additional averaging over space is necessary for convergence of our statistics (see Appendix A.6). The normalised structure functions $\overline{(\delta u'_j)^2} / \overline{\epsilon'}^{2/3}$ are therefore calculated by averaging over available points in the field of view in 150, 000 velocity field samples in this field of view. For two-point statistics, there are between 1.2×10^7 and 1.9×10^9 points available for convergence, depending on two-point separation vector, using both space and time averaging as explained in section 4.3.2.

Given that 7.10 implies $\langle \overline{(\delta u'_j)^2} / \overline{\epsilon'}^{2/3} \rangle = \langle C_j \rangle r^{2/3} F_j(\theta, \phi)$, we plot in figures 13a, 13b, 13c and 13d the compensated structure functions $\langle \overline{(\delta u'_x)^2} / \overline{\epsilon'}^{2/3} \rangle r^{-2/3}$ ($j = 1$) versus r_x/D (figure 13a) and versus r_z/D (figure 13b) and $\langle \overline{(\delta u'_z)^2} / \overline{\epsilon'}^{2/3} \rangle r^{-2/3}$ ($j = 3$) versus r_x/D (figure 13c) and versus r_z/D (figure 13d). This is the intermediate range data collapse suggested by 7.10 for all four configurations considered here. The dependence on r_x represents the dependence on r for $\theta = \pi/2$ and $\phi = 0$ whereas the dependence on r_z represents the dependence on r for $\theta = \pi/2$ and $\phi = \pi/2$. The average turbulence dissipation rate $\langle \overline{\epsilon'} \rangle$ varying by a factor larger than 4 across our four different configurations (see Table 3), figure 13 suggests that the collapse of the compensated structure functions in figure 13 is satisfactory. The exponent of the power law dependence of these structure functions on r_x and r_z (in an expected intermediate range of scales much smaller than $R = D/2$) appears close to but not exactly 2/3 and seems to vary a little around 2/3 from plot to plot in figure 13. The theory presented above and yielding equations 7.7 and 7.10 may be a leading order theory with different higher order corrections for different j components. Such corrections are beyond the scope of the present paper, but noting from the plots in figure 13 that there may be opposite corrections to the 2/3 scaling, we now consider the r_x and r_z dependencies of the normalized structure function $\langle \overline{(\delta u'^2_x + \delta u'^2_z)} / \overline{\epsilon'}^{2/3} \rangle$. Equation 7.10 implies

$$\langle \overline{(\delta u'^2_x + \delta u'^2_z)} / \overline{\epsilon'}^{2/3} \rangle = r^{2/3} [\langle C_1 \rangle F_1(\theta, \phi) + \langle C_3 \rangle F_3(\theta, \phi)]. \tag{7.11}$$

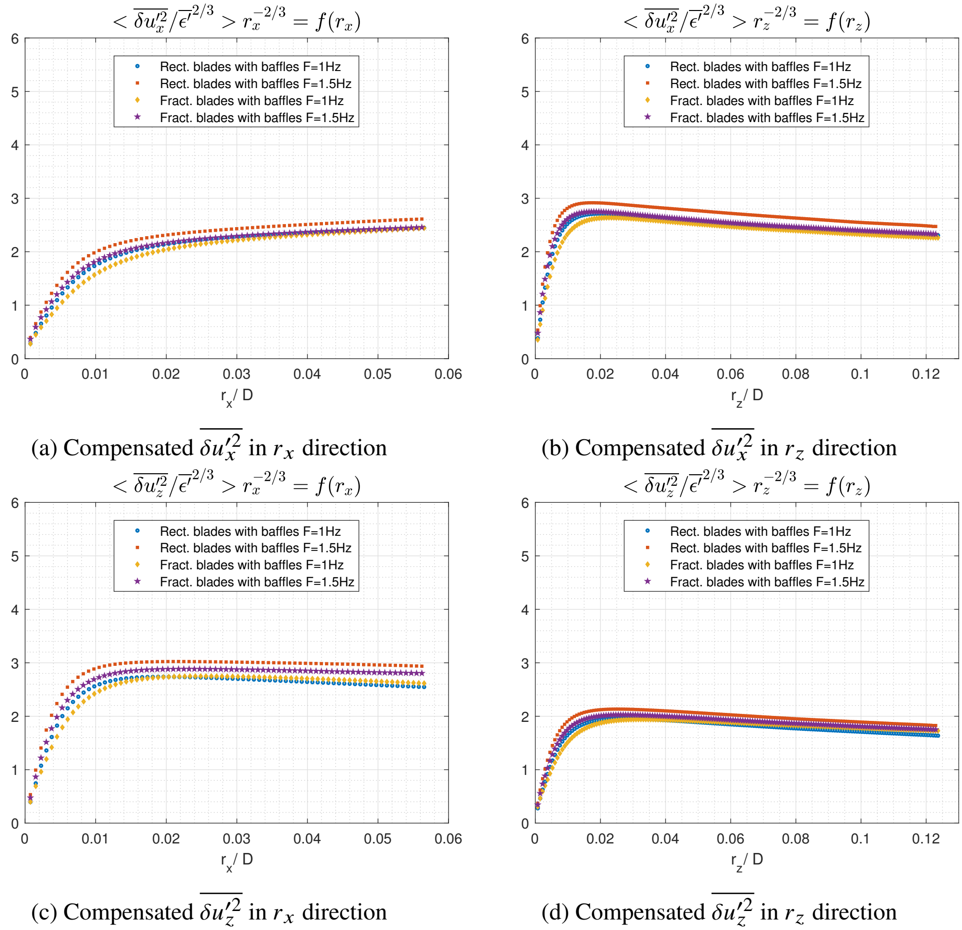

(a) Compensated $\overline{\delta u_x'^2}$ in r_x direction

(b) Compensated $\overline{\delta u_x'^2}$ in r_z direction

(c) Compensated $\overline{\delta u_z'^2}$ in r_x direction

(d) Compensated $\overline{\delta u_z'^2}$ in r_z direction

Figure 13: Compensated structure functions

This compensated normalised structure function is presented in figure 14 as a function of r_x/D (i.e. r/D for $\theta = \pi/2$ and $\phi = 0$) in one plot and of r_z/D (i.e. r/D for $\theta = \pi/2$ and $\phi = \pi/2$) in the other. Once again, the resulting collapse of the structure functions for the four different configurations is acceptable given the wide variation of $< \overline{\epsilon'} >$ from one configuration to the other. To look at the power law scaling more finely, we estimate the logarithmic slopes of $S \equiv \langle \overline{(\delta u_x'^2 + \delta u_z'^2)} / \overline{\epsilon'}^{2/3} \rangle$ versus both r_x and r_z, i.e. $\frac{dlogS}{dlogr_x}$ and $\frac{dlogS}{dlogr_z}$, which we plot versus r_x and r_z respectively in figures 15a and 15b. A well-defined plateau appears in both directions for $r_x, r_z \ll R = D/2$ which confirms the power-law behavior of S. The value of the plateau is the power-law exponent and it is slightly different in the two directions: it lies between $2/3 \approx 0.66$ and 0.7 in the r_x direction, which is very close to the theory's prediction but between 0.5 and 0.6 in the r_z direction which is further away from it.

We must leave it for future study to determine whether the deviation from $n = 2/3$ that we observe in the vertical r_z direction is a finite Reynolds number effect or whether it results from deviations from outer and/or inner isotropic similarity of second order structure functions. The good agreement with $n = 2/3$ in the r_x direction is nevertheless encouraging and so, in the following section, we use $n = 2/3$ in conjunction with an analysis of the

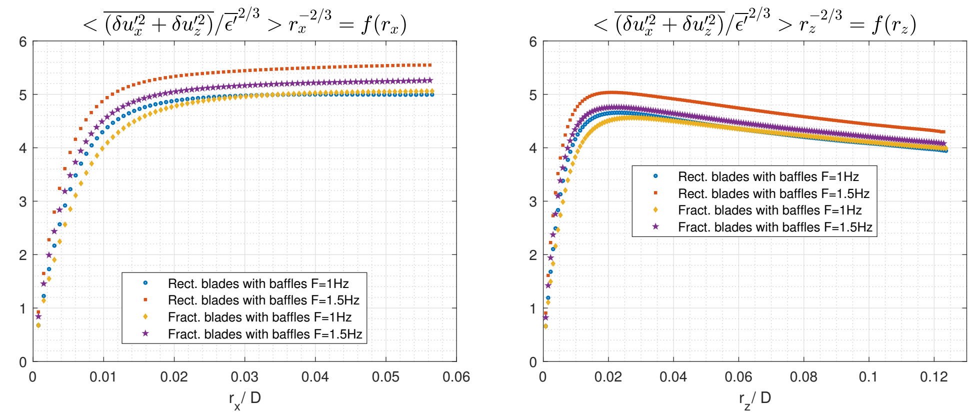

(a) r_x direction (b) r_z direction

Figure 14: Compensated structure function $\overline{(\delta u_x'^2 + \delta u_z'^2)}$

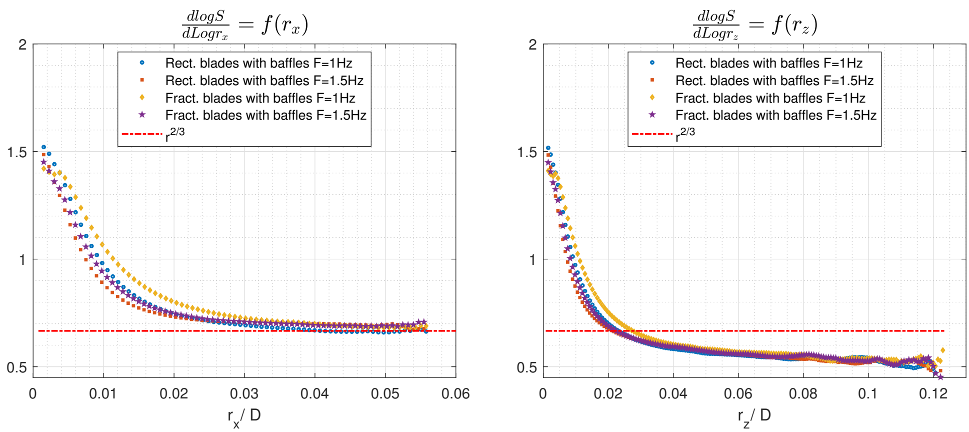

(a) r_x direction (b) r_z direction

Figure 15: Logarithmic slope of $S \equiv \langle \overline{(\delta u_x'^2 + \delta u_z'^2)}/\overline{\epsilon'}^{2/3} \rangle$

small-scale energy budget to predict the relations between l_I and l_O and between V_{I2} and V_{O2}. Perhaps more importantly, though, this analysis also leads to predictions concerning non-linear interscale and interspace turbulent energy transfer rates which do not critically depend on the value of the exponent n and which we also subject to experimental checks.

8. Small-scale turbulent energy budgets

Following Chen & Vassilicos (2022) who assume that regions exist in the flow where the non-linear and non-local dynamics of the small scale turbulence are similar at different places within the region, we now introduce, for such a region, inner and outer similarity forms for every term on the left hand side of equation 6.1.

Outer similarity for $|\boldsymbol{r}| >> l_I$:

$$\nabla_{\boldsymbol{X}}.(\overline{\boldsymbol{u_X}'|\boldsymbol{\delta u}'|^2}) = \frac{V_{OX}^3(\boldsymbol{X})}{l_O} f_{OX}\left(\frac{\boldsymbol{r}}{l_O}\right) \tag{8.1}$$

$$\nabla_{\boldsymbol{r}}.(\overline{\boldsymbol{\delta u}'|\boldsymbol{\delta u}'|^2}) = \frac{V_{O3}^3(\boldsymbol{X})}{l_O} f_{O3}\left(\frac{\boldsymbol{r}}{l_O}\right) \tag{8.2}$$

$$2\nabla_{\boldsymbol{X}}.\overline{(\boldsymbol{\delta u}'\delta p')} = \frac{V_{Op}^3(\boldsymbol{X})}{l_O} f_{Op}\left(\frac{\boldsymbol{r}}{l_O}\right) \tag{8.3}$$

Inner similarity for $|\boldsymbol{r}| << l_O$*:*

$$\nabla_{\boldsymbol{X}}.(\overline{\boldsymbol{u_X}'|\boldsymbol{\delta u}'|^2}) = \frac{V_{IX}^3(\boldsymbol{X})}{l_I} f_{IX}\left(\frac{\boldsymbol{r}}{l_I}\right) \tag{8.4}$$

$$\nabla_{\boldsymbol{r}}.(\overline{\boldsymbol{\delta u}'|\boldsymbol{\delta u}'|^2}) = \frac{V_{I3}^3(\boldsymbol{X})}{l_I} f_{I3}\left(\frac{\boldsymbol{r}}{l_I}\right) \tag{8.5}$$

$$2\nabla_{\boldsymbol{X}}.\overline{(\boldsymbol{\delta u}'\delta p')} = \frac{V_{Ip}^3(\boldsymbol{X})}{l_I} f_{Ip}\left(\frac{\boldsymbol{r}}{l_I}\right) \tag{8.6}$$

The characteristic velocities V_{OX}, V_{O3}, V_{Op}, V_{IX}, V_{I3}, V_{Ip} depend explicitly on $\boldsymbol{X}$ but are independent of $\boldsymbol{r}$ and f_{OX}, f_{O3}, f_{Op}, f_{IX}, f_{I3}, f_{Ip} are dimensionless functions which do not depend explicitly on $\boldsymbol{X}$ within the similarity region. Statistical homogeneity is the special case where $f_{OX} = f_{Op} = f_{IX} = f_{Ip} = 0$ and the characteristic velocities are independent of $\boldsymbol{X}$.

As in the previous section, we expect the outer characteristic velocities to be independent of viscosity but the inner characteristic velocities to depend on it. The ratios of outer to inner characteristic velocities are therefore functions of local Reynolds number Re_O, i.e. $V_{IX}/V_{OX} = g_X(Re_O, \boldsymbol{X})$, $V_{I3}/V_{O3} = g_3(Re_O, \boldsymbol{X})$, $V_{Ip}/V_{Op} = g_p(Re_O, \boldsymbol{X})$, these functions approaching zero as Re_O tends to infinity.

Following the approach we took in section 7, we can replace the hypothesis of similarity by a hypothesis of isotropic similarity for terms on the left hand side of equation 6.1. For the two terms not involving pressure fluctuations, this refined hypothesis states that $\frac{\partial}{\partial r_i}\overline{u'_{Xi}(\delta u'_j)^2}$ and $\frac{\partial}{\partial r_i}\overline{\delta u'_i(\delta u'_j)^2}$ (without summation over i and without summation over j) have an inner and an outer similarity form for every $i, j = 1, 2, 3$. Only $i, j = 1, 3$ are accessible to our 2D2C PIV measurements and we therefore decompose the interscale transfer rate in two sub-terms, both of which have an inner and an outer similarity form: $\frac{\partial}{\partial r_x}\overline{[\delta u'_x(\delta u'^2_x + \delta u'^2_z)]} + \frac{\partial}{\partial r_z}\overline{[\delta u'_z(\delta u'^2_x + \delta u'^2_z)]}$ which is accessible to our 2D2C PIV and $\frac{\partial}{\partial r_x}\overline{[\delta u'_x(\delta u'^2_y)]} + \frac{\partial}{\partial r_z}\overline{[\delta u'_z(\delta u'^2_y)]} + \frac{\partial}{\partial r_y}\overline{[\delta u'_y(\delta u'^2_x + \delta u'^2_y + \delta u'^2_z)]}$ which is not. For example,

$$\frac{\partial}{\partial r_x}\overline{[\delta u'_x(\delta u'^2_x + \delta u'^2_z)]} + \frac{\partial}{\partial r_z}\overline{[\delta u'_z(\delta u'^2_x + \delta u'^2_z)]} = \frac{V_{O3}^3(\boldsymbol{X})}{l_O} F_{O3}\left(\frac{\boldsymbol{r}}{l_O}\right) \tag{8.7}$$

for $|\boldsymbol{r}| \gg l_I$ and

$$\frac{\partial}{\partial r_x}\overline{[\delta u'_x(\delta u'^2_x + \delta u'^2_z)]} + \frac{\partial}{\partial r_z}\overline{[\delta u'_z(\delta u'^2_x + \delta u'^2_z)]} = \frac{V_{I3}^3(\boldsymbol{X})}{l_I} F_{I3}\left(\frac{\boldsymbol{r}}{l_I}\right) \tag{8.8}$$

for $|\boldsymbol{r}| \ll l_O$. The function F_{O3} is not the same as the function f_{O3} and the function F_{I3} is not the same as the function f_{I3}.

We do the same for the interspace transfer rate $\nabla_{\boldsymbol{X}}.(\overline{\boldsymbol{u_X}'|\boldsymbol{\delta u}'|^2})$ which we also decompose in two sub-terms, both of which have an inner and an outer similarity form. For the sub-term which is accessible to our 2D2C PIV, for example, we therefore write

$$\frac{\partial}{\partial r_x}\overline{[u'_{Xx}(\delta u_x'^2+\delta u_z'^2)]}+\frac{\partial}{\partial r_z}\overline{[u'_{Xz}(\delta u_x'^2+\delta u_z'^2)]}=\frac{V_{OX}^3(\boldsymbol{X})}{l_O}F_{OX}\left(\frac{\boldsymbol{r}}{l_O}\right) \tag{8.9}$$

for $|\boldsymbol{r}| \gg l_I$ and

$$\frac{\partial}{\partial r_x}\overline{[u'_{Xx}(\delta u_x'^2+\delta u_z'^2)]}+\frac{\partial}{\partial r_z}\overline{[u'_{Xz}(\delta u_x'^2+\delta u_z'^2)]}=\frac{V_{IX}^3(\boldsymbol{X})}{l_I}F_{IX}\left(\frac{\boldsymbol{r}}{l_I}\right) \tag{8.10}$$

for $|\boldsymbol{r}| \ll l_O$. Again, the function F_{OX} is not the same as the function f_{OX} and the function F_{IX} is not the same as the function f_{IX}.

8.1. *Outer balance*

Using the outer similarity forms 8.1, 8.2 and 8.3, Chen & Vassilicos (2022) have shown that the outer form of the small-scale energy balance 6.1 for $|\boldsymbol{r}| \gg l_I$ tends to

$$\frac{V_{OX}^3}{V_{O2}^3}f_{OX}(\boldsymbol{r}/l_O)+\frac{V_{O3}^3}{V_{O2}^3}f_{O3}(\boldsymbol{r}/l_O)+\frac{V_{Op}^3}{V_{O2}^3}f_{Op}(\boldsymbol{r}/l_O)=-C_\epsilon \tag{8.11}$$

as $Re_O \to \infty$, where the dissipation coefficient C_ϵ is defined on the basis of the turbulence dissipation scaling $\overline{\epsilon'} \sim V_{O2}^3/l_O$. This scaling follows from the hypothesis (often refered to as zeroth law of turbulence) that the turbulence dissipation rate is independent of the fluid's viscosity at large enough Reynolds number, hence $\overline{\epsilon'} = C_\epsilon V_{O2}^3/l_O$ where C_ϵ is independent of Reynolds number but can depend on $\boldsymbol{X}$ and boundary/forcing conditions. It follows from 8.11 that

$$V_{OX} \sim V_{O3} \sim V_{Op} \sim C_\epsilon^{1/3} V_{O2} \tag{8.12}$$

which means that all three velocities V_{OX}, V_{O3} and V_{Op} are the same function of $\boldsymbol{X}$ as $C_\epsilon^{1/3}V_{O2}$. (The independence of C_ϵ on $\boldsymbol{r}$ which is required to go from (8.11) to (8.12) is valid without any restriction on spatial gradients of turbulent dissipation: the only requirement is that the second order spatial derivative of turbulent dissipation should be small compared to $\overline{\epsilon'}/l_O^2$).

8.2. *Inner balance*

Using the inner similarity forms 8.4, 8.5 and 8.6, Chen & Vassilicos (2022) have shown that the inner form of the small-scale energy balance 6.1 for $|\boldsymbol{r}| \ll l_O$ tends to

$$g_X^3 g_l^{-1} f_{IX}(\boldsymbol{r}/l_I)+g_3^3 g_l^{-1} f_{I3}(\boldsymbol{r}/l_I)+g_p^3 g_l^{-1} f_{Ip}(\boldsymbol{r}/l_I)=-1+C_\epsilon^{-1}Re_O^{-1}g_2^2 g_l^{-2}\boldsymbol{\nabla}^2_{\mathbf{r}/l_I} f_{I2}(\boldsymbol{r}/l_I) \tag{8.13}$$

as $Re_O \to \infty$, where $\boldsymbol{\nabla}^2_{\mathbf{r}/l_I}$ is the Laplacian with respect to $\boldsymbol{r}/l_I$ and where $Re_O^{-1}g_2^2 g_l^{-2}$ is independent of Reynolds number. They obtained this result without considering the possibility of explicit dependencies of the functions g_X, g_3, g_p, g_l on $\mathbf{X}$ but it can be checked that their result remains intact if such dependencies are taken into account. Writing

$$g_2^2(Re_O,\boldsymbol{X})g_l^{-2}(Re_O,\boldsymbol{X}) = A_3(\boldsymbol{X})Re_O \tag{8.14}$$

in terms of a dimensionless coefficient A_3 which can depend on $\boldsymbol{X}$ (but not on $\boldsymbol{r}$ and viscosity), we note that equation 8.13 is viable only if $g_X^3 g_l^{-1}$, $g_3^3 g_l^{-1}$, $g_p^3 g_l^{-1}$ and A_3/C_ϵ are all independent of $\boldsymbol{X}$. Incidentally, the explicit $\mathbf{X}$-dependence of the functions g_2 and g_l and the constraint $A_3/C_\epsilon = Const$ independent of $\boldsymbol{X}$ cancel the need for the theoretical readjustments in the Appendix of Chen & Vassilicos (2022).

With 7.6 and the exponent $n = 2/3$ obtained theoretically in section 7, equation 8.14 implies $g_l \sim Re_O^{-3/4}$, therefore

$$l_I \sim l_O Re_O^{-3/4} \tag{8.15}$$

where the coefficient of proportionality can, in principle, be a function of $\boldsymbol{X}$. Using equation 8.14 once again leads to

$$V_{I2} \sim V_{O2} Re_O^{-1/4} \tag{8.16}$$

where the coefficient of proportionality is also, in principle, a function of $\boldsymbol{X}$. One notes the resemblance of l_I and V_{I2} with the Kolmogorov length and velocity scales. However, these forms of l_I and V_{I2} have been obtained in an explicitely non-homogeneous context with hypotheses which, unlike those of Kolmogorov (see Frisch (1995), Pope (2000) and section 2 of Chen & Vassilicos (2022)), are adapted to non-homogeneous non-equilibrium turbulence. Note that we use the value $2/3$ of the exponent n only to derive 8.15 and 8.16, nothing else in this paper, and that 8.15 and 8.16 are not used to derive anything in the paper either.

8.3. *Intermediate scalings*

The turbulence dissipation scaling $\overline{\epsilon'} = C_\epsilon V_{O2}^3/l_O$ and 8.12 imply

$$\overline{\epsilon'} \sim V_{O3}^3/l_O \sim V_{OX}^3/l_O \sim V_{Op}^3/l_O \tag{8.17}$$

where the proportionality coefficients are independent of $\boldsymbol{X}$ (and of course also independent of Re_O). One expects the non-linear terms to be part of the small-scale energy balance 8.13 which means that $g_X^3 g_l^{-1}$, $g_3^3 g_l^{-1}$ and $g_p^3 g_l^{-1}$ should be independent of Re_O in the limit $Re_O \to \infty$ and so we write, in this limit, $g_X^3 g_l^{-1} = B_X$, $g_3^3 g_l^{-1} = B_3$ and $g_p^3 g_l^{-1} = B_p$ where the dimensionless constants B_X, B_3, B_p are independent of $\boldsymbol{X}$, $\boldsymbol{r}$ and Re_O. With 8.17, the implication is

$$\overline{\epsilon'} \sim V_{I3}^3/l_I \sim V_{IX}^3/l_I \sim V_{Ip}^3/l_I \tag{8.18}$$

where, once again, the porportionality coefficients are independent of $\boldsymbol{X}$ and Re_O. Hence, in the intermediate range $l_I \ll |\boldsymbol{r}| \ll l_O$ where equation 8.1 matches equation 8.4, equation 8.2 matches equation 8.5 and equation 8.3 matches equation 8.6, we get $f_{OX}(\boldsymbol{r}/l_O) = B_X f_{IX}(\boldsymbol{r}/l_I)$, $f_{O3}(\boldsymbol{r}/l_O) = B_3 f_{I3}(\boldsymbol{r}/l_I)$ and $f_{Op}(\boldsymbol{r}/l_O) = B_p f_{Ip}(\boldsymbol{r}/l_I)$. These functions are therefore asymptotic constants in the intermediate range $l_I \ll |\boldsymbol{r}| \ll l_O$ as $Re_O \to \infty$, and therefore:

$$\boldsymbol{\nabla}_X.(\overline{\boldsymbol{u}_X'|\delta\boldsymbol{u}'|^2}) \sim \overline{\epsilon'}, \tag{8.19}$$

$$\boldsymbol{\nabla}_r.(\overline{\delta\boldsymbol{u}'|\delta\boldsymbol{u}'|^2}) \sim \overline{\epsilon'} \tag{8.20}$$

and

$$2\boldsymbol{\nabla}_X.\overline{(\delta\boldsymbol{u}'\delta p')} \sim \overline{\epsilon'} \tag{8.21}$$

in that range.

The dimensionless coefficients of proportionality in 8.19, 8.20 and 8.21 are independent of $\boldsymbol{r}$, independent of Reynolds number and independent of $\boldsymbol{X}$ in the similarity region of the flow considered. They add up to -1 asymptotically as $Re_O \to \infty$.

The same procedure applied to equations 8.7 and 8.8 on the one hand and equations 8.9

and 8.10 on the other yields

$$\frac{\partial}{\partial X_x}\overline{[u'_{Xx}(\delta u_x'^2 + \delta u_z'^2)]} + \frac{\partial}{\partial X_z}\overline{[u'_{Xz}(\delta u_x'^2 + \delta u_z'^2)]} \sim \overline{\epsilon'} \tag{8.22}$$

and

$$\frac{\partial}{\partial r_x}\overline{[\delta u'_x(\delta u_x'^2 + \delta u_z'^2)]} + \frac{\partial}{\partial r_z}\overline{[\delta u'_z(\delta u_x'^2 + \delta u_z'^2)]} \sim \overline{\epsilon'} \tag{8.23}$$

in the intermediate range $l_I \ll |\boldsymbol{r}| \ll l_O$ as $Re_O \to \infty$. The dimensionless coefficients of proportionality in these two relations are also independent of $\boldsymbol{r}$, Reynolds number and $\boldsymbol{X}$.

Note that our analysis does not reveal the signs of the various constants of proportionality in the five proportionality relations above. These signs are important, in particular for the interscale transfer rate as its sign can discriminate between transfer from small to large scales (forward cascade) or from large to small scales (inverse cascade). The last two proportionalities are the ones which are accessible to our 2D2C PIV measurements. For them, our measurements can establish whether the proportionality constants are well defined and, if they are, whether they are negative or positive.

Before moving to our energy transfer measurements, we note that the hypothesis of inner-outer equivalence for turbulence dissipation introduced by Chen & Vassilicos (2022) and used in section 7 can now be seen to be a consequence of Reynolds number-independence of turbulence dissipation, outer and inner similarities and the natural assumption $V_{I3} = C_I(\mathbf{X})V_{I2}$ where the dimensionless coefficient $C_I(\mathbf{X})$ is independent of Re_O and $\boldsymbol{r}$. Using $\overline{\epsilon'} = C_\epsilon(\mathbf{X})V_{O2}^3/l_O$ and the first proportionality in 8.18 (which follows from inner and outer similarities), one then obtains the inner-outer equivalence in the form $C_\epsilon(\mathbf{X})V_{O2}^3/l_O \sim C_I^3(\mathbf{X})V_{I2}^3/l_I$ with a proportionality coefficient that is independent of $\mathbf{X}$ and Re_O. (It also follows that $C_\epsilon(\mathbf{X})/C_I^3(\mathbf{X})$ is independent of $\mathbf{X}$).

8.4. *Energy transfer rate measurements*

The quantities obtained from our 2D2C PIV and presented in this sub-section require high spatial resolution, in particular for the estimation of the turbulence dissipation rate, and a high number of samples for convergence of third order statistics. Averaging over time is not enough for such convergence (see Appendix A.6). We therefore calculate spatial averages of both sides of proportionalities 8.22 and 8.23 given that they are the consequences of our theory that can be tested by our 2D2C PIV. In figures 16 and 17 we plot the normalised interscale transfer rate term $\frac{\partial}{\partial r_x}\langle\overline{[\delta u'_x(\delta u_x'^2 + \delta u_z'^2)]}\rangle/\langle\overline{\epsilon'}\rangle + \frac{\partial}{\partial r_z}\langle\overline{[\delta u'_z(\delta u_x'^2 + \delta u_z'^2)]}\rangle/\langle\overline{\epsilon'}\rangle$ and the normalised interspace transfer rate term $\frac{\partial}{\partial r_x}\langle\overline{[u'_{Xx}(\delta u_x'^2 + \delta u_z'^2)]}\rangle/\langle\overline{\epsilon'}\rangle + \frac{\partial}{\partial r_z}\langle\overline{[u'_{Xz}(\delta u_x'^2 + \delta u_z'^2)]}\rangle/\langle\overline{\epsilon'}\rangle$ (we recall that the brackets $\langle\ldots\rangle$ are averages over $\boldsymbol{X}$ in the plane of our field of view). Our theory predicts that an intermediate range of scales exists where these two normalised terms are about constant, this constant being the same for different Reynolds numbers. The spread of Taylor length-based Reynolds numbers across our four experimental configurations is from 480 to 650, and the average turbulence dissipation rate varies by a factor of 4 across these configurations. The Taylor length λ depends on the turbulence dissipation rate and in Appendix A we explain how we calculate both of them and how we denoise the PIV data for this purpose. The value of the average turbulence dissipation rate is probably slightly underestimated and this uncertainty is not taken into account in the error bars shown in figures 16 and 17. The spatial resolutions for all four configurations are given in Table 1.

The normalised energy transfer terms are plotted versus r_x/λ in figures 16a and 17a and versus r_z/λ in figures 16b and 17b. We normalise the components r_x and r_z of the vector $\mathbf{r}$ by λ because of the important role that λ has been shown to play in the separation length scale dependence of the interscale transfer rate in decaying homogeneous turbulence (Obligado & Vassilicos (2019), Meldi & Vassilicos (2021)) and in fully developed turbulent channel flow (Apostolidis *et al.* (2023)). We find (figure 16) that the interscale transfer rate is negative for all observed scales in both directions r_x and r_z and all four configurations. This suggests a non-linear interscale turbulent energy transfer that is perdominantly from large to small scales, i.e. that the turbulence cascade is forward on average. The 2D2C PIV measurements also appear to support our theory's prediction that a range of scales exists where the interscale transfer rate is proportional to the turbulence dissipation rate and independent of two-point separation length. Indeed, for the four configurations, $\frac{\partial}{\partial r_x}\langle\overline{[\delta u'_x(\delta u'^2_x + \delta u'^2_z)]}\rangle/\langle\overline{\epsilon'}\rangle + \frac{\partial}{\partial r_z}\langle\overline{[\delta u'_z(\delta u'^2_x + \delta u'^2_z)]}\rangle/\langle\overline{\epsilon'}\rangle$ appear to collapse within error bars around a constant value between 0.35 and 0.45 in the range $\lambda/2 \leqslant r_x \leqslant 2\lambda$ and around a constant value between 0.4 and 0.5 in the range $\lambda/2 \leqslant r_z \leqslant 5\lambda$. Beyond these values of r_x and r_z statistical convergence visibly weakens. The Taylor length takes values between $3.7mm$ and $4.9mm$ across our four configurations and the field of view of our PIV is $27mm \times\ 28mm$, hence we cannot access values of r_x/λ and r_z/λ larger than those in the plots of figure 16 and 17 (to avoid symmetry problems, we only used the right half of our field of view in the x-direction).

Whilst the negative sign of the average interscale transfer rate and its proportionality with the average turbulence dissipation rate over a range of scales are similar to Kolmogorov's prediction for the average interscale transfer rate in high Reynolds number statistically homogeneous stationary turbulence (Frisch (1995), Pope (2000), section 2 of Chen & Vassilicos (2022)), the constant of proportionality is not Kolmogorov equilibrium's -1 but significantly smaller. This difference may of course be accounted for by the difference between $\frac{\partial}{\partial r_x}\langle\overline{[\delta u'_x(\delta u'^2_x + \delta u'^2_z)]}\rangle/\langle\overline{\epsilon'}\rangle + \frac{\partial}{\partial r_z}\langle\overline{[\delta u'_z(\delta u'^2_x + \delta u'^2_z)]}\rangle/\langle\overline{\epsilon'}\rangle$ and $\boldsymbol{\nabla_r}.(\langle\overline{\boldsymbol{\delta u'}|\boldsymbol{\delta u'}|^2}\rangle)/\langle\overline{\epsilon'}\rangle$ and/or the Reynolds number not being large enough in case that this constant of proportionality has finite Reynolds number corrections. However, the results in figures 17a and 17b make it clear that the turbulence studied here is significantly non-homogeneous at the scales where $\frac{\partial}{\partial r_x}\langle\overline{[\delta u'_x(\delta u'^2_x + \delta u'^2_z)]}\rangle/\langle\overline{\epsilon'}\rangle + \frac{\partial}{\partial r_z}\langle\overline{[\delta u'_z(\delta u'^2_x + \delta u'^2_z)]}\rangle/\langle\overline{\epsilon'}\rangle$ is about constant. Indeed, these figures show that the normalised interspace transfer rate term $\frac{\partial}{\partial X_x}\langle\overline{[u'_{Xx}(\delta u'^2_x + \delta u'^2_z)]}\rangle/\langle\overline{\epsilon'}\rangle + \frac{\partial}{\partial X_z}\langle\overline{[u'_{Xz}(\delta u'^2_x + \delta u'^2_z)]}\rangle/\langle\overline{\epsilon'}\rangle$ is very significantly non-zero and in fact positive over all accessible length-scales in both directions r_x and r_z for all four configurations. These consistent positive values mean that there is a leaving average turbulent flux which takes small-scale turbulent kinetic energy out of the field of view at all accessible length scales. In fact, $\frac{\partial}{\partial X_x}\langle\overline{[u'_{Xx}(\delta u'^2_x + \delta u'^2_z)]}\rangle/\langle\overline{\epsilon'}\rangle$ dominates this interspace transfer rate (see figure 18) and $\frac{\partial}{\partial X_z}\langle\overline{[u'_{Xz}(\delta u'^2_x + \delta u'^2_z)]}\rangle/\langle\overline{\epsilon'}\rangle$ is negligible if slightly negative. The small-scale turbulence energy is therefore transported out of the field of view by the turbulence predominantly in the horizontal direction.

For all four configurations, $\frac{\partial}{\partial X_x}\langle\overline{[u'_{Xx}(\delta u'^2_x + \delta u'^2_z)]}\rangle/\langle\overline{\epsilon'}\rangle + \frac{\partial}{\partial X_z}\langle\overline{[u'_{Xz}(\delta u'^2_x + \delta u'^2_z)]}\rangle/\langle\overline{\epsilon'}\rangle$, and $\frac{\partial}{\partial X_z}\langle\overline{[u'_{Xz}(\delta u'^2_x + \delta u'^2_z)]}\rangle/\langle\overline{\epsilon'}\rangle$ which dominates it, appear to collapse within error bars around a constant value between about 0.05 and 0.15 in the range $\lambda/2 \leqslant r_x \leqslant 2\lambda$ and around a similar constant value in the range $\lambda/2 \leqslant r_z \leqslant 5\lambda$ (see figures 17a and 17b and 18). We stress once again, that larger two-point separation scales are not accessible to our PIV and statistical convergence weakens at the larger values of r_x and r_z that we can access. Nevertheless, the results in figures 17a and 17b and figure 18 do not invalidate and may even arguably offer some support to our theory's prediction 8.22 for the interspace turbulence transfer rate.

To summarise, the parts of the interscale and of the interspace average turbulent transfer

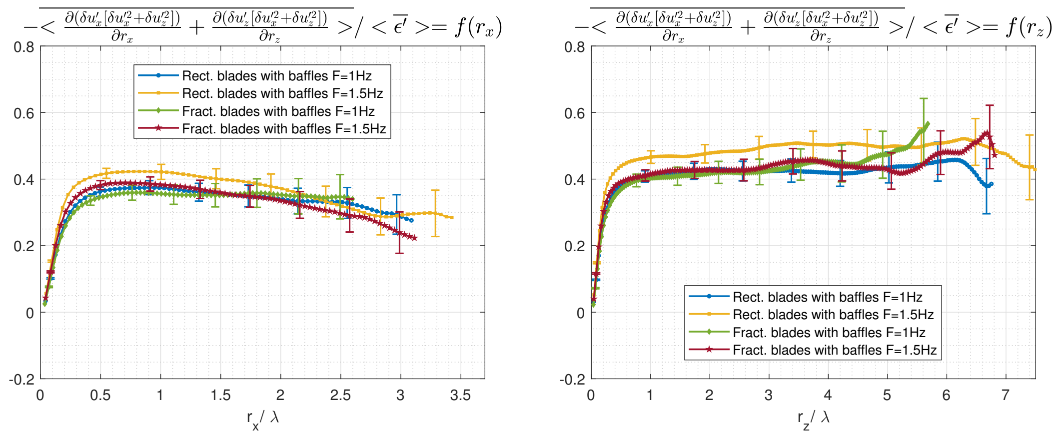

(a) r_x direction

(b) r_z direction

Figure 16: Interscale transfer rate estimate

rates that we can access appear to be independent of two-point separation scale and are proportional to the average turbulence dissipation rate over a more or less overlapping range of scales. The average turbulence dissipation rate and the Taylor length-scale collapse the two-point separation scale dependence of the accessible parts of the energy transfer rates for all four configurations tried here.

The average interscale transfer rate is negative, suggesting forward cascade, and the average interspace transfer rate is positive, suggesting outward turbulent transport of small-scale turbulence. This outward spatial turbulent flux is overwhelmingly in the x-direction. The non-homogeneity that it represents is present even at the smallest scales of the turbulence, in particular scales between $\lambda/2$ and 5λ. It is therefore not possible to apply the Kolmogorov equilibrium theory to the small scales of the present turbulent flows. However our non-equilibrium theory of non-homogeneous small-scale turbulence is able to account for some of our observations.

One can also analyse sub-terms of the part of the average interscale transfer rate that we measure. In figure 19, we plot $\frac{\partial}{\partial r_x}\langle\overline{[\delta u'_x(\delta u'^2_x + \delta u'^2_z)]}\rangle/\langle\overline{\epsilon'}\rangle$ and $\frac{\partial}{\partial r_z}\langle\overline{[\delta u'_z(\delta u'^2_x + \delta u'^2_z)]}\rangle/\langle\overline{\epsilon'}\rangle$ separately and see that they are both constant over the range of scales where their sum is constant and that they both contribute significantly to that sum but that the latter term is also significantly larger in magnitude than the former.

The magnitude of the accessible average interscale transfer rate is roughly 4 times larger than the magniture of the accessible average interspace transfer rate. Considering our measurements, our theory (in particular equation 8.21) and the small-scale energy balance 6.1 averaged over the field of view of our PIV, it is highly likely that the pressure-velocity term in that balance plays a dominant role at scales $|\mathbf{r}|$ larger than $\lambda/2$.

9. Large-scale turbulent energy budget

We do not apply the previous section's theoretical approach to the large-scale turbulent energy budget, equation 2.8, given that the two-point turbulence production rate P_X tends to the one-point turbulence production rate in the limit $\boldsymbol{r} \to 0$ and given the PIV evidence of section 5 suggesting that it is significantly non-zero at the smallest scales and does not

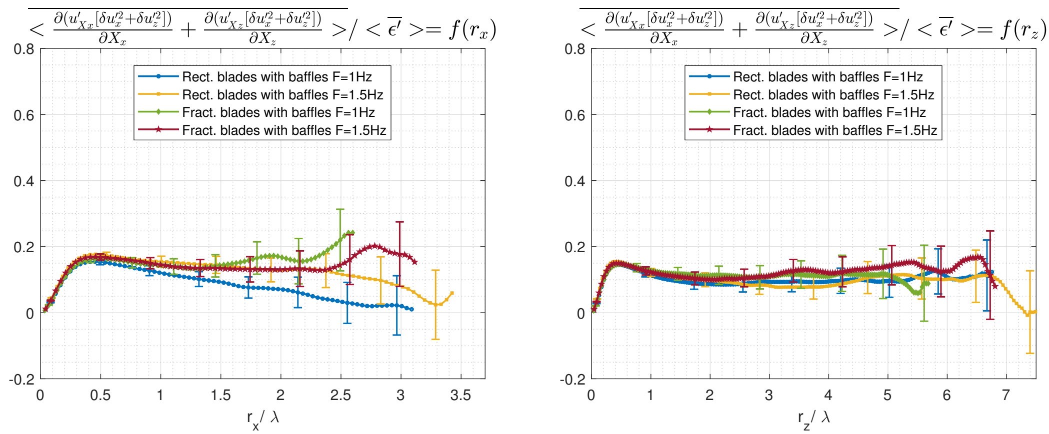

(a) r_x direction

(b) r_z direction

Figure 17: Interspace transport rate estimate

collapse with the average turbulence dissipation rate. Indeed, figure 9 shows that $\langle\widetilde{\widetilde{P_X}}\rangle/\langle\overline{\epsilon'}\rangle$ differs substantially for the regular and the fractal-like blades.

Furthermore, the spatio-temporal average of the part of the interspace turbulent transport rate of large-scale turbulence energy that is accessible to our 2D2C PIV, i.e. $\frac{\partial}{\partial X_x}[u'_{Xx}(u'^2_{Xx}+u'^2_{Xz})]+\frac{\partial}{\partial X_z}[u'_{Xz}(u'^2_{Xx}+u'^2_{Xz})]$, does not collapse with the average turbulence dissipation rate $\langle\overline{\epsilon'}\rangle$. This is clear in figures 20a and 20b which also show that the normalised spatio-temporal average $\frac{\partial}{\partial X_x}\langle\overline{[u'_{Xx}(u'^2_{Xx}+u'^2_{Xz})]}\rangle/\langle\overline{\epsilon'}\rangle+\frac{\partial}{\partial X_z}\langle\overline{[u'_{Xz}(u'^2_{Xx}+u'^2_{Xz})]}\rangle/\langle\overline{\epsilon'}\rangle$ may depend linearly on r_z for $r_z \geqslant \lambda/2$ and may be constant or linear with r_x for $r_x \geqslant \lambda/2$ depending on type of blade. This is very different behaviour from the average interspace turbulent transport rate of small-scale energy in figure 17.

Another important difference is the non vanishing value when $\boldsymbol{r} \to 0$ of the average interspace turbulent transport rate of large-scale energy (see figure 20). Indeed, when $\boldsymbol{r} \to 0$, this term converges to the space-time averaged one-point turbulent energy transport rate $<\overline{\boldsymbol{\nabla}.\boldsymbol{u}'|\boldsymbol{u}'|^2}>$. This one-point turbulence transport rate reflects the non-homogeneity of each particular configuration and there is no reason to expect it to collapse when normalised by dissipation. There is therefore no reason either to expect such a collapse for the average two-point interspace turbulent transport rate of large-scale energy at the smallest two-point separations. Consistently, the measurements suggest that such a collapse is in fact absent at all two-point separations tested (figure 20).

The indications are, therefore, that the large-scale turbulent energy budget 2.8 is very different from the small-scale turbulent energy budget and that a theory of the type developed in the previous section for the small-scale turbulent energy budget cannot be developed for the large-scale turbulent energy budget. Nevertheless, there is a kinematic relation between the rate with which large scales gain or lose turbulent energy to the small scales via non-linear turbulence interactions and the rate with which small scales gain or lose turbulent energy via such interactions. This is equation 3.2. Neglecting mean flow velocity differences and two-point turbulence production rates P_r and P^l_{Xr}, as appears to be possible in our PIV's field of view for small two-point separation lengths, equation 3.2 becomes

$$\boldsymbol{\nabla}_{\boldsymbol{r}}\cdot(\overline{\boldsymbol{\delta u}'|\boldsymbol{\delta u}'|^2})+\boldsymbol{\nabla}_{\boldsymbol{r}}\cdot(\overline{\boldsymbol{\delta u}'|\boldsymbol{u}_{\boldsymbol{X}}'|^2}) = 2\boldsymbol{\nabla}_{\boldsymbol{X}}\cdot(\overline{\boldsymbol{\delta u}'(\boldsymbol{\delta u}'\cdot\boldsymbol{u}'_{\boldsymbol{X}})}) \tag{9.1}$$

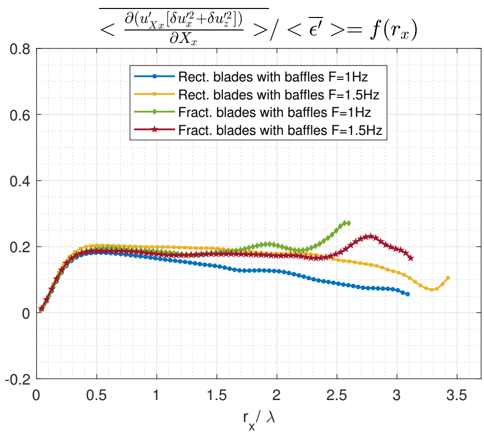

(a) Interspace transport rate $\frac{\partial}{X_x}$ contribution in r_x direction

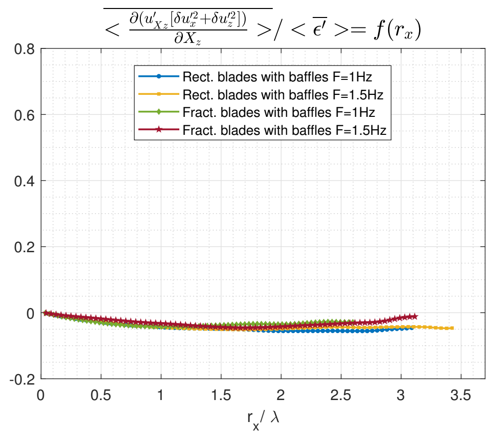

(b) Interspace transport rate $\frac{\partial}{X_z}$ contribution estimate in r_x direction

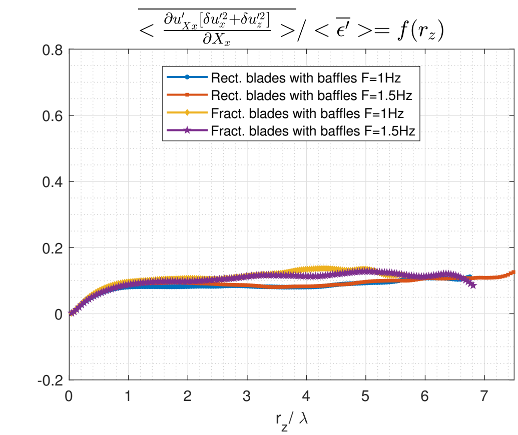

(c) Interspace transport rate $\frac{\partial}{X_x}$ contribution estimate in r_z direction

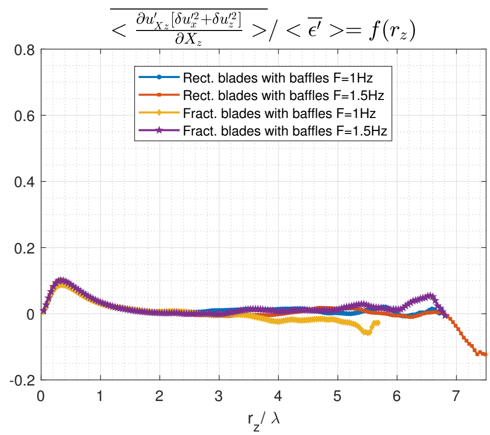

(d) Interspace transport rate $\frac{\partial}{X_z}$ contribution estimate in r_z direction

Figure 18: Interspace transport rate

where $\nabla_r \cdot (\overline{\boldsymbol{\delta u'}|\boldsymbol{u_X}'|^2})$ represents the rate with which large scales lose or gain turbulent energy to or from the small scales and $\nabla_r \cdot (\overline{\boldsymbol{\delta u'}|\boldsymbol{\delta u'}|^2})$ represents the rate with which small-scales gain or lose turbulent energy by the non-linear turbulence interactions (see also the complementary description of these transfer rates under equation 3.2). In general, and in the present flow in particular, the passage of turbulent energy from large to small scales (or vice versa) is not necessarily "impermeable" as energy can leak out of this cascade process because of non-homogeneities, in the present case by the spatial gradient term on the right hand side of 9.1.

In figures 21a and 21b we plot the spatio-temporal average of the part of $\nabla_r \cdot (\overline{\boldsymbol{\delta u'}|\boldsymbol{u_X}'|^2})$ that is accessible to our 2D2C PIV, namely $\frac{\partial}{\partial r_x}\langle[\delta u'_x(u'^2_{Xx}+u'^2_{Xz})]\rangle + \frac{\partial}{\partial r_z}\langle[\delta u'_z(u'^2_{Xx}+u'^2_{Xz})]\rangle$. We plot it normalised by $\langle\overline{\epsilon'}\rangle$ versus both r_x/λ and r_z/λ and we note that it collapses well for the four different configurations. Furthermore, it appears to have a constant value across the same ranges $\lambda/2 \leqslant r_x \leqslant 2\lambda$ and $\lambda/2 \leqslant r_z \leqslant 5\lambda$ where the part of the spatio-temporal average of $\nabla_r \cdot (\overline{\boldsymbol{\delta u'}|\boldsymbol{\delta u'}|^2})$ that is accessible to our PIV has an approximately collapsed

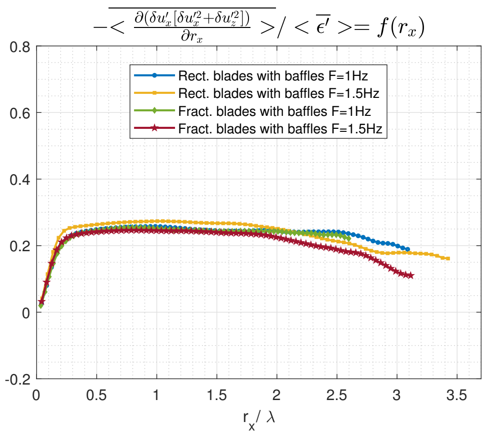

(a) Interscale transfer rate $\frac{\partial}{r_x}$ contribution in r_x direction

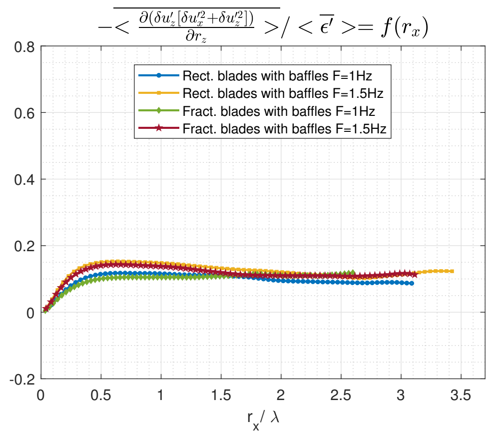

(b) Interscale transfer rate $\frac{\partial}{r_z}$ contribution estimate in r_x direction

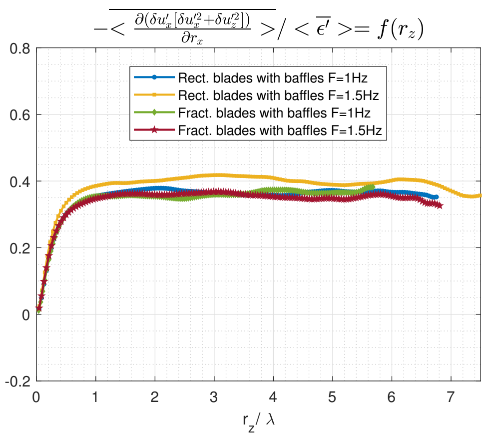

(c) Interscale transfer rate $\frac{\partial}{r_x}$ contribution estimate in r_z direction

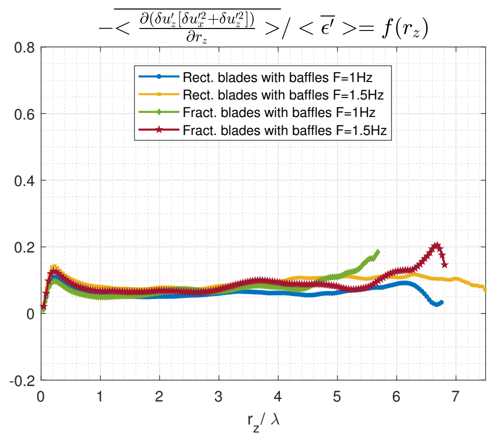

(d) Interscale transfer rate $\frac{\partial}{r_z}$ contribution estimate in r_z direction

Figure 19: Interscale transfer rate

constant value (figure 16). This suggests a strong link between these two turbulent energy transfer rates.

The positive constant value of $\frac{\partial}{\partial r_x}\langle\overline{[\delta u'_x(u'^2_{Xx}+u'^2_{Xz})]}\rangle/\langle\overline{\epsilon'}\rangle+\frac{\partial}{\partial r_z}\langle\overline{[\delta u'_z(u'^2_{Xx}+u'^2_{Xz})]}\rangle/\langle\overline{\epsilon'}\rangle$ (see figure 21) is slightly lower than the magnitude of the negative constant value of $\frac{\partial}{\partial r_x}\langle\overline{[\delta u'_x(\delta u'^2_x+\delta u'^2_z)]}\rangle/\langle\overline{\epsilon'}\rangle + \frac{\partial}{\partial r_z}\langle\overline{[\delta u'_z(\delta u'^2_x+\delta u'^2_z)]}\rangle/\langle\overline{\epsilon'}\rangle$ (see figure 16). If this experimental observation reflects a similar difference between $\boldsymbol{\nabla_r}.(\overline{\boldsymbol{\delta u'}|\boldsymbol{u_X}'|^2})$ and $\boldsymbol{\nabla_r}.(\overline{\boldsymbol{\delta u'}|\boldsymbol{\delta u'}|^2})$ then the interpretation will have to be that large scales lose energy to small scales but that the small scales receive more of the energy lost by the large ones because some energy is transported from elsewhere in physical space without changing scale. In the kinematic equation 9.1, this energy leak away from the interscale turbulent energy transfer process is accounted for by $2\boldsymbol{\nabla_X}.(\overline{\boldsymbol{\delta u'}(\boldsymbol{\delta u'}.\boldsymbol{u'_X})})$ which can be non-zero in non-homogeneous turbulence (or, more generally, by all the other terms present in equation 3.2 if they cannot be neglected).

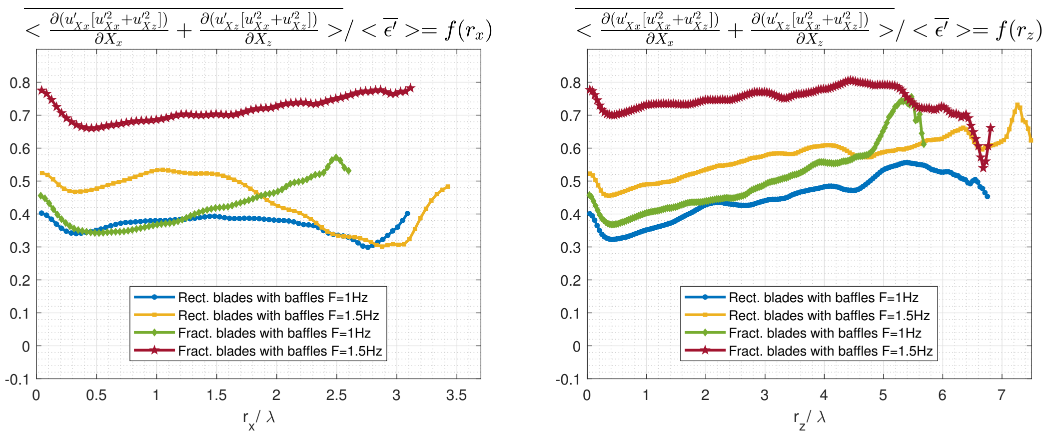

(a) r_x direction (b) r_z direction

Figure 20: Interspace transfer estimate of $\boldsymbol{u_X}^2$

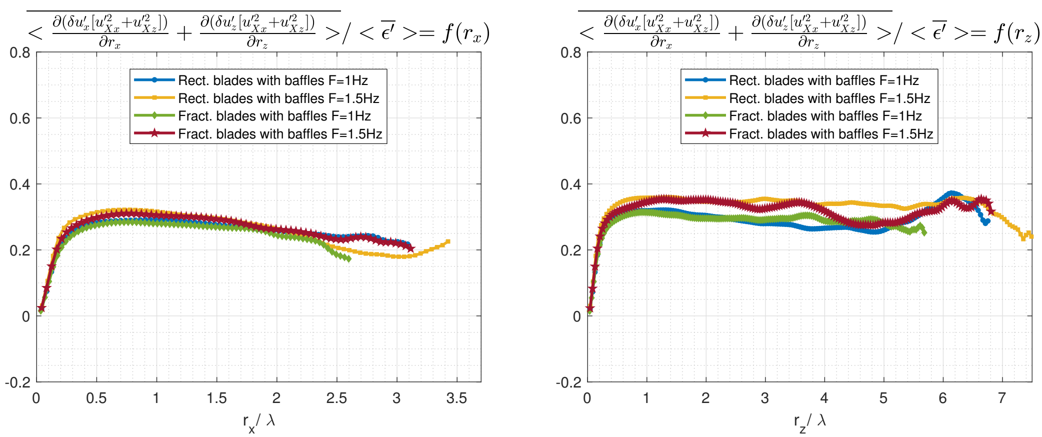

(a) r_x direction (b) r_z direction

Figure 21: Interscale transfer estimate of $\boldsymbol{u_X}^2$

The experimental results presented in figures 21a and 21b may be reflecting a proportionality

$$\nabla_{\boldsymbol{r}} \cdot <\delta \boldsymbol{u}' |\boldsymbol{u_X}'|^2 > \sim < \epsilon' > \tag{9.2}$$

which cannot be confirmed or invalidated with our 2D2C PIV. This proportionality concerns interscale energy transfer within the large-scale turbulent energy budget and is additional to the proportionalities 8.19, 8.20, 8.21 obtained in the previous section on the basis of the small-scale turbulent energy budget. The previous section's theory does not give the proportionality coefficients of these relations. In the following section we present an hypothesis which has the power, if and when valid, to determine some such proportionality coefficients.

10. A local small-scale homogeneity hypothesis

We consider statistically stationary non-homogeneous turbulence by comparison to the case of statistically homogeneous non-stationary turbulence which we addressed in section 3 (equations 3.3 to 3.8). Statistical stationarity is meant in the Lagrangian sense of following the mean flow, i.e. $\overline{\boldsymbol{u_X}}.\boldsymbol{\nabla_X}\frac{1}{2}\overline{|\boldsymbol{\delta u'}|^2} = 0 = \overline{\boldsymbol{u_X}}.\boldsymbol{\nabla_X}\frac{1}{2}\overline{|\boldsymbol{u'_X}|^2}$. This is indeed the case in the present flows because the mean flow velocity is vertical (i.e. in the z direction) and the turbulence varies mainly in the horizontal direction. With this statistical stationarity and by considering scales $|\mathbf{r}|$ large enough to neglect viscous diffusion, fluctuating energy equations 2.4 and 2.8 become, respectively,

$$\begin{aligned}&\boldsymbol{\delta\overline{u}}.\boldsymbol{\nabla_r}\frac{1}{2}\overline{|\boldsymbol{\delta u'}|^2} - P_r - P^s_{Xr} + \boldsymbol{\nabla_X}\cdot\left(\overline{\boldsymbol{u_X}'\frac{1}{2}|\boldsymbol{\delta u'}|^2} + \overline{\boldsymbol{\delta u'}\delta p'}\right)\\ &\approx -\boldsymbol{\nabla_r}.(\overline{\boldsymbol{\delta u'}\frac{1}{2}|\boldsymbol{\delta u'}|^2}) - \frac{\nu}{4}\overline{\frac{\partial u_i'^+}{\partial\zeta_k^+}\frac{\partial u_i'^+}{\partial\zeta_k^+}} - \frac{\nu}{4}\overline{\frac{\partial u_i'^-}{\partial\zeta_k^-}\frac{\partial u_i'^-}{\partial\zeta_k^-}}\end{aligned} \tag{10.1}$$

and

$$\begin{aligned}&\boldsymbol{\delta\overline{u}}.\boldsymbol{\nabla_r}\frac{1}{2}\overline{|\boldsymbol{u'_X}|^2} - P_X - P^l_{Xr} + \boldsymbol{\nabla_X}\cdot\left(\overline{\boldsymbol{u_X}'\frac{1}{2}|\boldsymbol{u_X}'|^2} + \overline{\boldsymbol{u_X}'p'_X}\right)\\ &\approx -\boldsymbol{\nabla_r}.(\overline{\boldsymbol{\delta u'}\frac{1}{2}|\boldsymbol{u_X}'|^2}) - \frac{\nu}{4}\overline{\frac{\partial u_i'^+}{\partial\zeta_k^+}\frac{\partial u_i'^+}{\partial\zeta_k^+}} - \frac{\nu}{4}\overline{\frac{\partial u_i'^-}{\partial\zeta_k^-}\frac{\partial u_i'^-}{\partial\zeta_k^-}}\end{aligned} \tag{10.2}$$

We formulate an hypothesis of local homogeneity as a parallel to Kolmogorov's small-scale stationarity hypothesis (see section 3). Whereas most terms on the left hand side of equation 10.2 do not tend to 0 as $\boldsymbol{r}$ tends to 0, the left hand side of 10.1 does tend to 0 in that limit. The local small-scale homogeneity hypothesis that we make is the hypothesis that in the limit of increasing Reynolds number, the magnitude of $\boldsymbol{\delta\overline{u}}.\boldsymbol{\nabla_r}\frac{1}{2}\overline{|\boldsymbol{\delta u'}|^2} - P_r - P^s_{Xr} + \boldsymbol{\nabla_X}\cdot\left(\overline{\boldsymbol{u_X}'\frac{1}{2}|\boldsymbol{\delta u'}|^2} + \overline{\boldsymbol{\delta u'}\delta p'}\right)$ is increasingly smaller than the local time-averaged turbulence dissipation rate at small enough scales $|\boldsymbol{r}|$. With this hypothesis, and with the approximation $\frac{\nu}{4}\overline{\frac{\partial u_i'^+}{\partial\zeta_k^+}\frac{\partial u_i'^+}{\partial\zeta_k^+}} + \frac{\nu}{4}\overline{\frac{\partial u_i'^-}{\partial\zeta_k^-}\frac{\partial u_i'^-}{\partial\zeta_k^-}} \approx \overline{\epsilon'}$ which is acceptable at small enough $|\boldsymbol{r}|$, the small-scale turbulent energy balance 10.1 simplifies to

$$\boldsymbol{\nabla_r}.(\overline{\boldsymbol{\delta u'}|\boldsymbol{\delta u'}|^2}) \approx -\overline{\epsilon'} \tag{10.3}$$

in an intermediate range of scales large enough to neglect viscous diffusion but small enough to neglect small-scale non-homogeneity. This balance incorporates the proportionality 8.20 but also sets the proportionality constant to -1. The similarity hypotheses required to obtain 8.20 are weaker than the local small-scale homogeneity hypothesis introduced here. A priori, they can be valid even if and when the local small-scale homogeneity hypothesis is not. When $\boldsymbol{\delta\overline{u}}$, P_r and P^s_{Xr} are negligible at small enough $|\boldsymbol{r}|$, as appears to be the case in the flow regions considered here, the local small-scale homogeneity hypothesis implies that the magnitude of $\boldsymbol{\nabla_X}\cdot\left(\overline{\boldsymbol{u_X}'\frac{1}{2}|\boldsymbol{\delta u'}|^2} + \overline{\boldsymbol{\delta u'}\delta p'}\right)$ is increasingly small compared to $\overline{\epsilon'}$ with increasing Reynolds number for small enough values of $|\boldsymbol{r}|$. It may be that, as the Reynolds number tends to infinity, 8.20 tends to 10.3 thereby recovering Kolmogorov's scale-by-scale equilibrium for homogeneous turbulence at small enough scales and implying that this Kolmogorov equilibrium is a very particular case of 8.20. However, it is not clear how such a statement could be established at the current time and the foreseeable future.

We now use the kinematic relation 9.1, but we could also use its more general form 3.2 if we did not want to neglect $\delta\overline{\boldsymbol{u}}$, P_r and P^l_{Xr} from the outset. From 9.1 and 10.3 follows

$$\nabla_{\boldsymbol{r}}.\overline{\delta\boldsymbol{u}'|\boldsymbol{u}'_{\boldsymbol{X}}|^2} \approx \overline{\epsilon'} + 2\nabla_{\boldsymbol{X}} \cdot (\overline{\delta\boldsymbol{u}'(\delta\boldsymbol{u}' \cdot \boldsymbol{u}'_{\boldsymbol{X}})}) \tag{10.4}$$

which is the analogue for stationary non-homogeneous turbulence of the Germano-Hosokawa relation 3.7 for homogeneous non-stationary (in fact freely decaying) turbulence.

Finally, the analogue of 3.8 for stationary non-homogeneous turbulence is obtained from 10.4 and 10.2 and it is

$$-P_X - P^l_{Xr} + \nabla_{\boldsymbol{X}} \cdot \left(\overline{\boldsymbol{u_X}'\frac{1}{2}|\boldsymbol{u_X}'|^2} + \overline{\boldsymbol{u_X}'p'_X} + \overline{\delta\boldsymbol{u}'(\delta\boldsymbol{u}' \cdot \boldsymbol{u}'_{\boldsymbol{X}})} \right) \approx -\overline{\epsilon'}. \tag{10.5}$$

Like equation 10.3, equations 10.4 and 10.5 hold in an intermediate range of scales large enough to neglect viscous diffusion and small enough to neglect small-scale non-homogeneity. Note that equation 10.5 identifies a statistic characterising non-homogeneity which is proportional to $\overline{\epsilon'}$ with proportionality coefficient -1. This statistic is not captured by the non-equilibrium theory of non-homogeneous turbulence of section 8. In this case, the hypothesis of local small-scale homogeneity makes a prediction concerning turbulence non-homogeneity which is not accessible to the theory of section 8.

11. Conclusion

We have studied a turbulent flow region under rotating blades in a baffled container where the baffles break the rotation in the flow. The evidence from our 2D2C PIV supports the view that, within our PIV's field of view, two-point production makes a negligible contribution to the small-scale energy equation 2.4 over a range of small two-point separation lengths. In the absence of such production, we may assume the non-linear and non-local dynamics of the small-scale turbulence to be effectively the same at different places. We have therefore made the similarity hypothesis that every term in the non-homogeneous but statistically stationary scale-by-scale (two-point) small-scale energy balance 6.1 has the same dependence on two-point separation at different positions **X** if rescaled by **X**-local velocity and length scales. Following the theory of Chen & Vassilicos (2022) we have introduced such similarity hypotheses for both inner and outer scales and have considered intermediate matchings. We have also improved the theory (i) by deriving the inner-outer equivalence hypothesis of Chen & Vassilicos (2022) for turbulence dissipation from a more intuitively natural hypothesis and (ii) by taking explicit account of non-homogeneity in the inner to outer velocity ratios, thereby extending the theory's applicability range and removing the need for the theoretical adjustments in the Appendix of Chen & Vassilicos (2022).

This non-equilibrium theory of non-homogeneous small-scale turbulence predicts that an intermediate range of length-scales exists where the interscale turbulence transfer rate, the two-point interspace turbulence transport rate and the two-point pressure gradient velocity correlation term in equation 6.1 are all proportional to the turbulence dissipation rate. Given the limitations of 2D2C PIV we have been able to measure only parts (truncations) of the interscale turbulence transfer rate and the two-point interspace turbulence transport rate in equation 6.1. This has forced us to introduce inner and outer hypotheses of isotropic similarity applicable to the truncations accessible to our measurements. With these hypotheses (which should not be confused with hypotheses of isotropy) the theory leads to the same predictions for the 2D2C PIV-truncated interscale turbulence transfer rate and two-point interspace turbulence transport rate in equation 6.1. Our 2D2C PIV measurements suggest that these truncations may indeed be independent of two-point separation scale and be proportional to the average turbulence dissipation rate over a more or less overlapping range of scales as predicted by the theory. The PIV-truncated two-point interspace turbulence transport rate is significantly non-zero, thereby reflecting both the presence of small-scale non-homogeneity and the absence of Kolmogorov scale-by-scale equilibrium. Its proportionality with the turbulence dissipation rate is evidence that small-scale non-homogeneity and non-equilibrium do actually obey general rules.

The PIV-truncated average interscale transfer rate of small-scale turbulent energy is negative, suggesting forward cascade if the corresponding full (non-truncated) average interscale transfer rate has the same sign, and the PIV-truncated average interspace turbulent transfer rate of small-scale turbulence energy is positive, suggesting outward turbulent transport of small-scale turbulence if the corresponding full (non-truncated) average interspace turbulent transfer rate is also positive.

We have also applied hypotheses of inner and outer similarity as well as inner and outer isotropic similarity to second order structure functions of turbulent fluctuating velocities. Inner-outer intermediate matching has led to the prediction of power law dependencies on turbulence dissipation rate and two-point separation length with power law exponent $n = 2/3$. The 2D2C PIV has provided support for this Kolmogorov-like value of the exponent in the r_x direction but not in the r_z direction where the PIV suggests an exponent n between 0.5 and 0.6. Future studies should investigate whether rotation, even if effectively faint within our field of view because of the rotation-breaking effect of the baffles, may require similarity forms in terms of more than one outer length scale l_O and more than one inner length scale l_I, depending on direction. The value of the exponent n impacts only the Reynolds number dependencies of l_I/l_O and V_I/V_O and has no direct impact on the other predictions of the theory. The exponent $n = 2/3$ implies the Kolmogorov-like scalings 8.15 and 8.16.

The large-scale turbulent energy budget 2.8 is very different from the small-scale turbulent energy budget 2.4 both in terms of production and interspace turbulence transport which are both non-zero in the limit of zero two-point separation lengths when the turbulence is inhomogeneous. We have therefore not applied to 2.8 the similarity approach that we applied to 2.4. However, we have taken advantage of the kinematic relation which exists between the rate with which large scales gain or lose turbulent energy to the small scales via non-linear turbulence interactions (present in 2.8) and the rate with which small scales gain or lose turbulent energy via such interactions (present in 2.4). The PIV-truncated part of the rate with which large scales gain or lose turbulent energy to the small scales has turned out to be approximately independent of two-point separation scale and proportional to the average turbulence dissipation rate over the same range of scales where the PIV-truncated interscale transfer rate in 2.4) exhibites the same behaviour. However, these two transfer rates do not balance, which suggests that the transfer of turbulent energy from large to small scales (or vice versa) may not be "impermeable" in the sense that energy may be leaking out of this cascade process because of non-homogeneities, in the present case by the spatial gradient term on the right hand side of 9.1.

Our non-equilibrium theory of non-homogeneous turbulence does not give the proportionality coefficients in 8.19, 8.20 and 8.21. We have therefore introduced a local small-scale homogeneity hypothesis in section 10 as a space analogue of Kolmogorov's small-scale stationarity hypothesis but do not have criteria, at this stage, for the validity of this small-scale homogeneity hypothesis. If and when this new hypothesis may hold (perhaps in the limit of infinite Reynolds numbers?) the coefficient of proportionality in 8.20 will be -1.

Acknowledgements. The CNRS Research Federation on Ground Transports and Mobility, in articulation with the Elsat2020 project supported by the European Community, the French Ministry of Higher Education and Research, the Hauts de France Regional Council are acknowledged for the founding of the PIV equipements used in this study. We thank Jean-Philippe Laval for providing the DNS data used in appendix A.4

Funding. This work was directly supported by JCV's Chair of Excellence CoPreFlo unded by I-SITE-ULNE (grant number R-TALENT-19-001-VASSILICOS), MEL (grant number CONVENTION_219_ESR_06) and Region Hauts de France (grant number 20003862). Funded by the European Union (ERC, NoStaHo, 101054117). Views and opinions expressed are however those of the author(s) only and do not necessarily reflect those of the European Union or the European Research Council. Neither the European Union nor the granting authority can be held responsible for them.

Declaration of interests. The authors report no conflict of interest.

Data availability statement. The data that support the findings of this study are available upon request.

Appendix A. Computation of the turbulence parameters

The following conventions are used to compute the different turbulent parameters.

A.1. *Dissipation*

The axisymmetric dissipation formulation is used (George & Hussein (1991)) where the rotation axis is z (A 1). The dissipation is averaged both in space and time to obtain a converged estimate over the field of view. The notation $< . >$ is used for space averaging and $\overline{(.)}$ for time averaging.

$$< \overline{\epsilon'} >= \nu < \overline{\left(-\left(\frac{\partial u_z'}{\partial z}\right)^2 + 2\left(\frac{\partial u_z'}{\partial x}\right)^2 + 2\left(\frac{\partial u_x'}{\partial z}\right)^2 + 8\left(\frac{\partial u_x'}{\partial x}\right)^2\right)} >. \tag{A 1}$$

Different estimates are tested to check the results' robustness with respect to the choice estimate. One of them is defined in equation A 2 and evaluated in table 4 after signal denoising (method explained in the next paragraph):

$$< \overline{\epsilon_\tau'} >= \frac{\nu}{3} < \overline{\left(2 \times 15\left(\frac{\partial u_x'}{\partial x}\right)^2 + 15\left(\frac{\partial u_z'}{\partial z}\right)^2\right)} >. \tag{A 2}$$

The results are different by less than 10% but more importantly the evolution from one configuration to the other is consistent. Therefore, the results' variation does not seems to be significantly dependent on the estimate choice so that dissipation scalings can be evaluated accurately. However, the value itself might contains some uncertainty.

The dissipation computation from experimental data is difficult because PIV introduces random noise during measurements. This noise significantly contaminates the dissipation (Foucaut *et al.* (2021)). Indeed, the turbulent energy is small at small scales so that noise can dominate at these scales. In the paper mentioned, the product of the derivatives used to compute dissipation is overestimated by 70% before denoising. The best way to denoise dissipation is to perform the experiment with two different PIV set-ups so that the noise of both measurements are decorrelated. The product of the derivatives obtained from the two systems cancel the random noise contribution (equation A 3). Indeed, the noise is not correlated with the true signal and the noise of the two set-ups is decorrelated so it cancels out once averaged.

$$
\begin{aligned}
&< \frac{\partial u'}{\partial x}|_{s1} \times \frac{\partial u'}{\partial x}|_{s2} > \\
&=< \widehat{\frac{\partial u'}{\partial x}}|_{s1} \times \widehat{\frac{\partial u'}{\partial x}}|_{s2} > + < \beta_{s1} \times \widehat{\frac{\partial u'}{\partial x}}|_{s2} > + < \widehat{\frac{\partial u'}{\partial x}}|_{s1} \times \beta_{s2} > + < \beta_{s1} \times \beta_{s2} > \\
&=< \widehat{\frac{\partial u'}{\partial x}}|_{s1} \times \widehat{\frac{\partial u}{\partial x}}|_{s2} >
\end{aligned} \tag{A 3}
$$

Where $< . >$ is used for realization averaging here, s_1 (resp. s_2) refers to system 1 (resp. system 2), β is the random PIV noise and $\widehat{(.)}$ refers to denoised data (i.e. without noise but with PIV interrogation window filtering effect).

This double measurement was not possible for this experiment because of practical limitations. Therefore, a simplified denoising method is used. The idea is to use the measurement's high resolution (in space or in time) and shift the two derivatives by a small offset. This method introduces a small filtering of the true signal but the noise cancels out. The experimental measurements are highly resolved in time so time denoising is used:

$$
\begin{aligned}
&< \frac{\partial u'}{\partial x}|_{t} \times \frac{\partial u'}{\partial x}|_{t+dt} > \\
&=< \widehat{\frac{\partial u'}{\partial x}}|_{t} \times \widehat{\frac{\partial u'}{\partial x}}|_{t+dt} > + < \beta_{t} \times \widehat{\frac{\partial u'}{\partial x}}|_{t+dt} > + \widehat{\frac{\partial u'}{\partial x}}|_{t} \times \beta_{t+dt} > + < \beta_{t} \times \beta_{t+dt} > \\
&=< \widehat{\frac{\partial u'}{\partial x}}|_{t} \times \widehat{\frac{\partial u'}{\partial x}}|_{t+dt} > \\
&\approx< \widehat{\frac{\partial u'}{\partial x}}|_{t} \times \widehat{\frac{\partial u'}{\partial x}}|_{t} >
\end{aligned} \tag{A 4}
$$

where β_t and β_{t+dt} are uncorrelated because the new particles entering the interrogation window (IW) at t +dt change the peak shape, so the peak fit random noise is then completely different. This method is valid if dt (the time increment between two velocity fields) is small enough so that the denoised quantities do not change significantly between two time steps but not too small (otherwise there would be no new particles inside the IW). In the experiments carried out, dt is chosen to have time resolved results which means the particle displacement between two frames is less than 10 pixels. The PIV processing (final pass) is done with a window size of 32 pixels $\times$ 32 pixels so that there is already a spatial filtering of the data. Therefore, the filtering introduced by shifting the two derivatives by a maximum of 10 pixels is comparable or smaller than the already existing PIV filtering so that the results should not change significantly. Therefore, this method can be used to denoise experimental data without losing too much information of the true signal. This method might however slightly underestimate the dissipation. The same procedure can also be used in space by selecting different points in the derivative, i.e. multiplying the derivative at x and at x+dx computed with a centred scheme, where dx is the vector spacing. As a 62% overlap is used, the four points used are separated by 36px which corresponds to a second filter which has about the same filter size as the IW.

The denoising process is tested both in space and in time to check the results consistency (table 4). The results are close so that the method seems to be reliable. There is a significant dissipation decrease associated to the denoising process (around a factor 2). These results seems to be consistent because the mixer PIV measurements are expected to be more noisy

	F (Hz)	$<\overline{\epsilon'}>$ (with noise)	$<\widehat{\overline{\epsilon'}}>$ (space method)	$<\widehat{\overline{\epsilon'}}>$ (time method)	$<\widehat{\overline{\epsilon'_\tau}}>$ (time method)
Rectangular blades	1	5.2E-03	3.5E-03	3.6E-03	3.7E-03
Rectangular blades	1.5	1.7E-02	1.1E-02	1.2E-02	1.3E-02
Fractal blades	1	4.2E-03	2.6E-03	2.4E-03	2.5E-03
Fractal blades	1.5	1.3E-02	8.2E-03	8.2E-03	8.6E-03

Table 4: Dissipation computation (m^2/s^3)

than typical air experiments. Indeed, this noise is amplified by the remaining presence of small air bubbles in water and the difficulty to obtain the optimal particle concentration linked to this high magnification measurement. These results underline also the importance to denoise dissipation. The energy spectrums and two-point statistics do not need to have the same denoising process because the noise is known to be present only at small scales. Therefore, only the small scale part of the results (large k in Fourier space or small r in two-point space) are contaminated by this PIV noise. Eventually, the PIV resolution affects significantly the dissipation results and a small underestimation is expected in our results as explained in section 4.3.1.

Overall, the dissipation computation is a difficult problem where resolution, noise and convergence affect significantly the results. For these experiments, the resolution is acceptable in several configurations which can be used for reference, the noise impact is removed through denoising process and the convergence is achieved through an averaging over 100,000 velocity fields (corresponding to 50,000 uncorrelated) and space averaging over the field of view. The dissipation estimate is expected to be slightly underestimated. For simplicity the notation $\widehat{(.)}$ is not used in the publication but all the dissipation results are denoised.

A.2. *Taylor micro scale and Taylor Reynolds number*

The following formulation of the Taylor micro-scale is used:

$$\lambda = \sqrt{\frac{15\nu}{\epsilon}}\sqrt{\frac{u_x'^2 + u_z'^2}{2}} \tag{A 5}$$

The value of the Taylor scale can vary significantly with the formulation choice. However, the variation from one configuration to the other should remain consistent whatever the formulation. The following formulation is also tested:

$$\widetilde{\lambda} = \sqrt{\frac{15\nu}{\epsilon}}\sqrt{\frac{2u_x'^2 + u_z'^2}{3}} \tag{A 6}$$

This formulation overestimates the value by a close to constant proportion between 20% and 25 % compared to A 5. The plots collapse is nearly unchanged when this later estimate is used to non-dimensionalize r.

The Reynolds number based on the Taylor length is calculated:

$$Re_\lambda = \frac{\lambda\sqrt{u_x'^2 + u_z'^2}}{\nu} \tag{A 7}$$

This number is used to quantify the turbulence development. The following formulation is also tested:

$$\widetilde{Re_\lambda} = \frac{\widetilde{\lambda}\sqrt{2u_x'^2 + u_z'^2}}{\nu} \tag{A 8}$$

This formulation overestimates the value by a close to constant proportion between 45% and 50% compared to A 7. This magnitude difference is significant but the main risk is to overestimate the Reynolds number. Therefore, the formulation with the smallest values is retained.

A.3. *Peak locking quantification*

The experimental PIV measurements introduce a random error which respect a Gaussian distribution law. This distribution law has a zero mean and usually a standard deviation around 0.1 - 0.2 px (Raffel *et al.* (2018)). It introduces also the peak locking systematic error as explained previously. This latter error can be quantified through the probability distribution function (PDF) of the particle displacement in pixel: $u_{pixel} - round(u_{pixel})$. A constant PDF means there is no peak locking. The results are presented in figure 22. Some peak-locking is observed in the results. This error is similar for all configurations and is more important in the x direction.

The peak locking error can be modeled as $-a.sin(2\pi(u_{true} - round(u_{true}))$ so that $u_{measured} = u_{true} - a.sin(2\pi(u_{true} - round(u_{true})) + \epsilon_{Gaussian}$, where $\epsilon_{Gaussian}$ is the random noise and u_{true} the true displacement with IW filtering effect. However, the peak locking can be estimated as $a.sin(2\pi(u_{measured} - round(u_{measured}))$ according to Cholemari (2007). The coefficient represents the peak-locking magnitude and it can be evaluated from experimental data using the previous approximation. A correction is added to the contaminated data until the PDF of the rounded part of the displacement is nearly flat. The coefficient a used for this correction gives a good estimate of the peak locking magnitude. For all configurations, the maximal value of a is estimated to be $0.02px$.
It means the peak locking error order of magnitude is around 10 times smaller than the Gaussian PIV noise. However, this error does not necessarily disappear when averaged because it is a systematic error. This is why the consequences of this phenomenon on the results of this study are quantified.

A.4. *Peak locking impact on spatial energy spectrums*

The peak locking impact on spatial energy spectrums is evaluated by introducing artificial peak locking into Direct Numerical Simulations (DNS).

The DNS dataset was computed by Jean-Philippe Laval from LMFL. It is a 512×512×512 pseudo-spectral periodic simulation with $Re_\lambda \approx 140$. The resolution is around 1.6η. The energy spectrum is computed directly from the simulation results and from the results affected by a modeled peak locking:

$$u_{peaklocking} = u_{simulation} - a \times sin(2\pi(u_{simulation} - round(u_{simulation})) \tag{A 9}$$

with $a = 0.02px$.

The results are presented in figure 23. The peak-locking does not have any consequence on the spatial energy spectrum except at the very high wavelengths where in reality it will be much more polluted by the PIV noise. Therefore, the experimental results can be used to compute energy spectrums without restrictions.

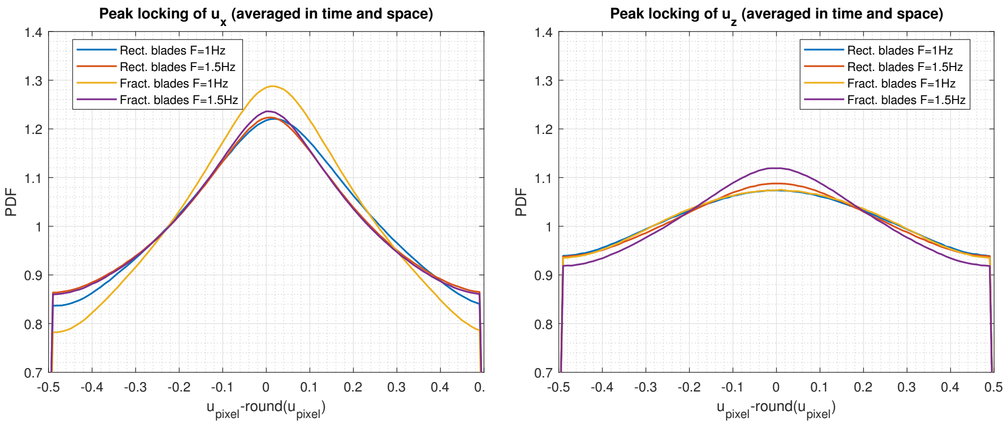

(a) u_x decimal part (b) u_z decimal part

Figure 22: Probability distribution function of the decimal part

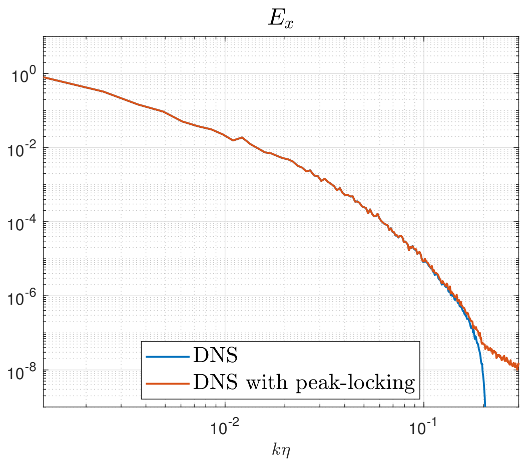

Figure 23: Peak locking impact on spatial energy spectrum from DNS.

A.5. *Peak-locking impact on two-point statistics*

The peak locking impact on averaged two-point statistics is quantified by introducing a peak locking correction in the experimental data. Then, we evaluate the results evolution after the correction. The correction defined in Cholemari (2007) is used:

$$u_{corrected} = u_{measured} + a_{estimated} \times sin(2\pi(u_{measured} - round(u_{measured})) \quad \text{(A 10)}$$

where a is estimated for each configuration in x and y direction.

The results are presented in figure 24. No difference is observed between the results with and without peak locking correction. Therefore, the experimental results can be used to compute two-point statistics without restrictions. The results presented in the publication do not contain peak locking correction.

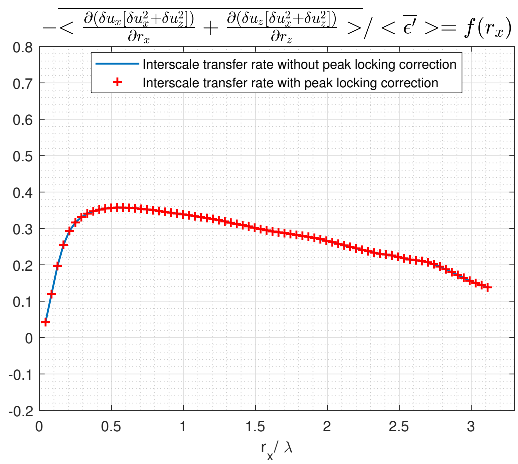

Figure 24: Peak-locking impact on energy interscale transfer rate

A.6. *Space averaging impact on results*

Structure functions are averaged in space to improve convergence as the results collapse is very sensitive to convergence. Therefore, the results are plotted in figure 25a, 25b, 25c and 25d without space averaging to check it does not affect results. Only one configuration is presented but it is representative of the four configurations. $V_I = V_O.R_O^{-1/4}$ and $l_I = l_O.R_O^{-3/4}$ are defined arbitrarily where $l_O = D$ and $V_O = \sqrt{\overline{u_x'^2} + \overline{u_z'^2}}$. However, it is important to note that V_I and l_I are nearly constant over the spatial domain with a variation of less than 3% for the two quantities. The error bars for these results are computed with classical convergence formula. The largest error bar of all positions is used and centered on the spatially averaged structure function (in red). The results collapse within error bars for $\overline{\delta u_x'^2}/V_I^2 = f(r_x)$, $\overline{\delta u_x'^2}/V_I^2 = f(r_z)$, $\overline{\delta u_z'^2}/V_I^2 = f(r_x)$ and $\overline{\delta u_z'^2}/V_I^2 = f(r_z)$, which confirms that space averaging does not distort the results and can be therefore used to improve convergence. These results are also consistent with the inner region structure functions' similarity assumed in equation 7.2. The outer region is not accessible with our dataset.

Third order statistics are even more difficult to converge than second order statistics. Therefore, space averaging is mandatory to converge results. The most critical quantity is the interspace transport as it is computed with space derivatives which can be affected by space averaging. The interspace transport averaged in time and space is compared to the same quantity averaged in time and in space for only one direction (z) but at different x locations (figure 26). The results are not well converged due to the number of points reduction. The shape of the non-converged functions at the different x positions seems to be consistent with the converged results averaged in space. Therefore, spatial averaging can be used to improve the results convergence without loss of information and without significant distortion of the results.

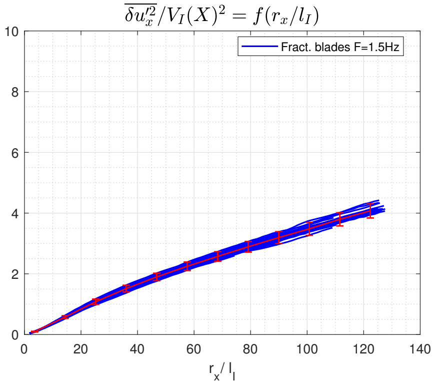

(a) Time averaged results of $\overline{\delta u_x'^2}/V_I^2$ in r_x direction at different spatial positions.
In red: $< \overline{\delta u_x'^2}/V_I^2 >$

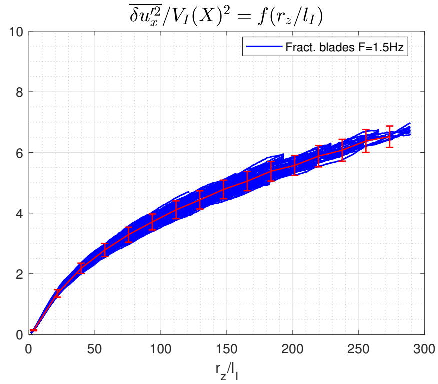

(b) Time averaged results of $\overline{\delta u_x'^2}/V_I^2$ in r_z direction at different spatial positions.
In red: $< \overline{\delta u_x'^2}/V_I^2 >$

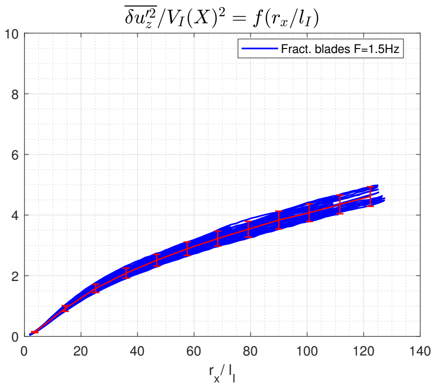

(c) Time averaged results of $\overline{\delta u_z'^2}/V_I^2$ in r_x direction at different spatial positions.
In red: $< \overline{\delta u_z'^2}/V_I^2 >$

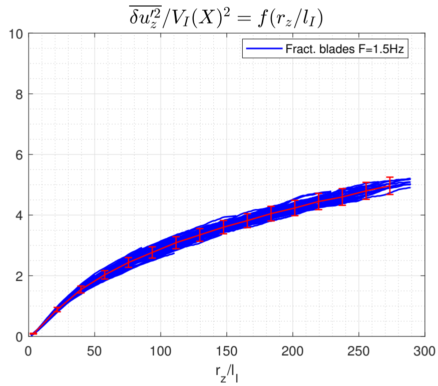

(d) Time averaged results of $\overline{\delta u_z'^2}/V_I^2$ in r_z direction at different spatial positions.
In red: $< \overline{\delta u_z'^2}/V_I^2 >$

Figure 25: Time averaged structure functions at different spatial locations

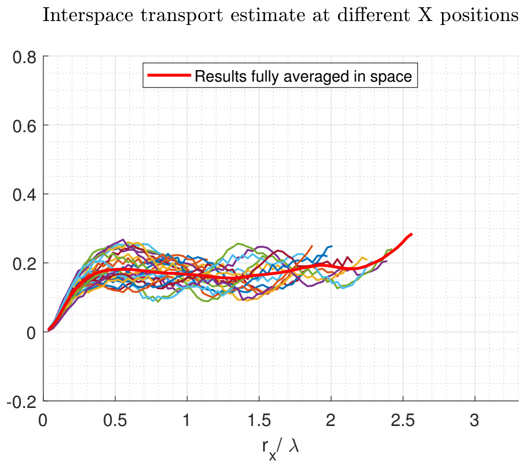

Figure 26: Space averaging impact on interspace transport

REFERENCES

Alves Portela, F., Papadakis, G. & Vassilicos, J. C. 2017 The turbulence cascade in the near wake of a square prism. *Journal of Fluid Mechanics* **825**.

Apostolidis, A, Laval, J P & Vassilicos, J C 2023 Turbulent cascade in fully developed 2 turbulent channel flow. *Journal of Fluid Mechanics* .

Baroud, Charles N., Plapp, Brendan B., She, Zhen-Su & Swinney, Harry L. 2002 Anomalous Self-Similarity in a Turbulent Rapidly Rotating Fluid. *Physical Review Letters* **88** (11).

Chen, J.G. & Vassilicos, J.C. 2022 Scalings of scale-by-scale turbulence energy in non-homogeneous turbulence. *Journal of Fluid Mechanics* **938**.

Cholemari, Murali R. 2007 Modeling and correction of peak-locking in digital PIV. *Experiments in Fluids* **42** (6).

Christensen, K. T. 2004 The influence of peak-locking errors on turbulence statistics computed from PIV ensembles. *Experiments in Fluids* **36** (3).

Foucaut, Jean Marc, George, William K., Stanislas, Michel & Cuvier, Christophe 2021 Optimization of a SPIV experiment for derivative moments assessment in a turbulent boundary layer. *Experiments in Fluids* **62** (12).

Frisch, Uriel 1995 *Turbulence: The Legacy of A. N. Kolmogorov*. Cambridge University Press.

George, William K. & Hussein, Hussein J. 1991 Locally axisymmetric turbulence. *Journal of Fluid Mechanics* **233**, publisher: Cambridge University Press.

Germano, M. 2007 The elementary energy transfer between the two-point velocity mean and difference. *Physics of Fluids* **19** (8), publisher: American Institute of Physics.

Hill, Reginald J. 2001 Equations relating structure functions of all orders. *Journal of Fluid Mechanics* **434**.

Hill, Reginald J. 2002 The Approach of Turbulence to the Locally Homogeneous Asymptote as Studied using Exact Structure-Function Equations ArXiv: physics/0206034.

Hosokawa, I. 2007 A Paradox concerning the Refined Similarity Hypothesis of Kolmogorov for Isotropic Turbulence. *Progress of Theoretical Physics* **118** (1).

Keane, R. D. & Adrian, R. J. 1991 Optimization of particle image velocimeters: II. Multiple pulsed systems. *Measurement Science and Technology* **2** (10).

Laizet, S., Nedić, J. & Vassilicos, J. C. 2015 Influence of the spatial resolution on fine-scale features in DNS of turbulence generated by a single square grid. *International Journal of Computational Fluid Dynamics* **29** (3-5).

Lavoie, P., Avallone, G., De Gregorio, F., Romano, G. P. & Antonia, R. A. 2007 Spatial resolution of PIV for the measurement of turbulence. *Experiments in Fluids* **43** (1).

Lecordier, B. & Trinité, M. 2004 Advanced PIV algorithms with Image Distortion Validation and Comparison using Synthetic Images of Turbulent Flow. In *Particle Image Velocimetry: Recent Improvements* (ed. M. Stanislas, J. Westerweel & J. Kompenhans). Berlin, Heidelberg: Springer.

Meldi, M. & Vassilicos, J. C. 2021 Analysis of Lundgren's matched asymptotic expansion approach to the K\'arm\'an-Howarth equation using the eddy damped quasinormal Markovian turbulence closure. *Physical Review Fluids* **6** (6), publisher: American Physical Society.

Nagata, Shinji 1975 Mixing: Principles and Applications.

Obligado, M. & Vassilicos, J. C. 2019 The non-equilibrium part of the inertial range in decaying homogeneous turbulence. *Europhysics Letters* **127** (6), publisher: EDP Sciences, IOP Publishing and Società Italiana di Fisica.

Pope, Stephen B. 2000 *Turbulent Flows*. Cambridge: Cambridge University Press.

Raffel, Markus, Willert, Christian E., Scarano, Fulvio, Kähler, Christian J., Wereley, Steve T. & Kompenhans, Jürgen 2018 *Particle Image Velocimetry: A Practical Guide*. Cham: Springer International Publishing.

Scarano, Fulvio 2001 Iterative image deformation methods in PIV. *Measurement Science and Technology* **13**.

Soria, Julio 1996 An investigation of the near wake of a circular cylinder using a video-based digital cross-correlation particle image velocimetry technique. *Experimental Thermal and Fluid Science* **12** (2).

Steiros, K., Bruce, P. J. K., Buxton, O. R. H. & Vassilicos, J. C. 2017*a* Effect of blade modifications on the torque and flow field of radial impellers in stirred tanks. *Physical Review Fluids* **2** (9).

Steiros, K., Bruce, P. J. K., Buxton, O. R. H. & Vassilicos, J. C. 2017*b* Power consumption and form drag of regular and fractal-shaped turbines in a stirred tank. *AIChE Journal* **63** (2).

Willert, C. E. & Gharib, M. 1991 Digital particle image velocimetry. *Experiments in Fluids* **10** (4).